

DESIGN AND IMPLEMENTATION OF MAGNETIC FIELD SENSORS FOR
BIOMEDICAL APPLICATIONS

A THESIS SUBMITTED TO
THE GRADUATE SCHOOL OF NATURAL AND APPLIED SCIENCES
OF
MIDDLE EAST TECHNICAL UNIVERSITY

ULAŞ CAN İNAN

IN PARTIAL FULFILLMENT OF THE REQUIREMENTS
FOR
THE DEGREE OF MASTER OF SCIENCE
IN
ELECTRICAL AND ELECTRONICS ENG.

FEBRUARY 2015

Approval of the thesis:

**DESIGN AND IMPLEMENTATION OF MAGNETIC FIELD SENSORS FOR
BIOMEDICAL APPLICATIONS**

submitted by **ULAŞ CAN İNAN** in partial fulfillment of the requirements for the degree of **Master of Science in Electrical and Electronics Eng. Department, Middle East Technical University** by,

Prof. Dr. Gülbin Dural
Dean, Graduate School of **Natural and Applied Sciences**

Prof. Dr. Gönül Turhan Sayan
Head of Department, **Electrical and Electronics Eng.**

Prof. Dr. Nevzat G. Gençer
Supervisor, **Electrical and Electronics Eng Dept, METU**

Examining Committee Members:

Prof. Dr. Murat Eyüboğlu
Electrical and Electronics Engineering Dept., METU

Prof. Dr. Nevzat G. Gençer
Electrical and Electronics Engineering Dept., METU

Assoc. Prof. Dr. Yeşim Serinağaoğlu
Electrical and Electronics Engineering Dept., METU

Assoc. Prof. Dr. Lale Alatan
Electrical and Electronics Engineering Dept., METU

Assoc. Prof. Dr. Süha Yağcıoğlu
Biophysics, Hacettepe University

Date: 10.02.2015

I hereby declare that all information in this document has been obtained and presented in accordance with academic rules and ethical conduct. I also declare that, as required by these rules and conduct, I have fully cited and referenced all material and results that are not original to this work.

Name, Last Name: ULAŞ CAN İNAN

Signature :

ABSTRACT

DESIGN AND IMPLEMENTATION OF MAGNETIC FIELD SENSORS FOR BIOMEDICAL APPLICATIONS

Can İnan, Ulaş

M.S., Department of Electrical and Electronics Eng.

Supervisor : Prof. Dr. Nevzat G. Gençer

February 2015, 85 pages

In this work, firstly the magnetic sensor types and their feasibility for biomedical applications are investigated. Then the air-cored induction coil sensor is chosen due to its advantages. Afterwards the usage of induction coils combined with amplifiers and connection types are studied. The biomedical applications requiring the use of magnetic field sensors are introduced. One of them, Lorentz Field Electrical Impedance Tomography (LFEIT) is explained in detail and experimental work is done for this application. In the second part, formulation of the magnetic sensor and the amplification circuitry, its frequency related components and frequency response is introduced. An optimization algorithm using MATLAB software is prepared to be able to determine the most sensitive disk shaped air-cored induction coil by its size parameters. This software is tested before moving further forward, according to the formulations given. After explaining the discrepancies caused by the problems encountered through the experimental process, an optimum induction coil sensor is designed for LFEIT application. The sensitivity and linearity of the system are analyzed. Two different amplifier configurations are used. First one includes AD797 as voltage amplifier and

the sensitivity of this system is measured to be 17.1 (V m/A). The amplification factor obtained is 20. The maximum deviation from linearity for this case is computed as %15.3. Second one includes two cascaded amplifiers namely, AD600 and AU-1291. The sensitivity of this configuration is measured as 5.45 (V m/A). The maximum deviation from linearity is computed as %2.7. Second configuration is preferred since with the use of cascaded amplifiers, the amplification is increased to 160000. Although the coil with the best sensitivity using the present equipment is wound, the performance of the sensor is still inadequate and it is concluded that better sensitivity is required. There are also other promising coil designs obtained using the software developed, however they are not wound yet. Still, the performance is not expected to increase significantly. A sensitivity of about 10^7 is itself a great challenge which cannot be overcome by adjusting the amplifier since the signal to noise ratio (SNR) does not improve and the signal to be observed remains smaller than the noise level. However the software providing the optimum coil parameters for a specific case is useful in more than one application. Furthermore it can be modified to optimize other coil types such as rectangular coil, flat-spiral coil etc. allowing a very wide range of possible sensor designs. Other than LFEIT, wireless power transfer application of magnetic sensors is also investigated. The conditions that maximizes the power transfer efficiency are studied. The same algorithm used in determining the coil size parameters with maximum sensitivity is also applied to find the coil with the optimum quality factor, which is the most important condition for obtaining the best efficiency in power transfer. Four coil wireless power transfer is chosen, designed and implemented to compare with the analytical results. The efficiency of the designed system is measured as %7.6. This value is increased to %39 by using litz wire at the windings instead of enamel copper wire.

Keywords: Magnetic Field Sensors, Biomedical Applications, LFEIT, Lorentz Field, Induction Coil, Coil design

ÖZ

BİYOMEDİKAL UYGULAMALARI İÇİN MANYETİK ALAN SENSÖR TASARIMI VE YAPIMI

Can İnan, Ulaş

Yüksek Lisans, Elektrik ve Elektronik Mühendisliği Bölümü

Tez Yöneticisi : Prof. Dr. Nevzat G. Gençer

Şubat 2015, 85 sayfa

Bu çalışmanın ilk kısmında, manyetik sensör türleri ve bunların biyomedikal uygulamalarında kullanılabilirliği araştırılmaktadır. Sağladığı avantajlar göz önünde bulundurularak hava çekirdekli endüksiyon bobini seçildi. Çalışmanın devamında endüksiyon bobini ile amplifikatör kombinasyonu ve bağlantı türleri incelendi. Manyetik alan sensörü kullanımı gerektiren biyomedikal uygulamaları tanıtıldı. Bunlardan biri, Lorentz Alanı Elektriksel Empedans Tomografisi detaylı bir şekilde açıklandı ve bu uygulama için deneysel çalışma gerçekleştirildi. İkinci kısımda manyetik sensör ve amplifikatör devresinin frekansa bağlı elemanları ve bunların frekansı cevabı, ayrıca ilgili formüller verildi. En hassas ölçümü yapabilecek disk şeklindeki hava çekirdekli endüksiyon bobininin boyut değişkenlerini belirlemek amacıyla MATLAB yazılımı kullanılarak bir optimizasyon algoritması geliştirildi. Daha fazla ilerlemeden önce bu yazılım, verilmiş olan formüllerden yararlanarak test edildi. Deneysel süreç boyunca karşılaşılan problemlerden doğan farklılıklar açıklandıktan sonra, LAEET uygulamasında kullanılmak üzere bir optimum endüksiyon bobini dizayn edildi. İki farklı

yükseltici düzeneği kullanıldı. Bunlardan birincisinde AD797 isimli voltaj yükselticisi bulunmaktadır ve bu sistemin duyarlılığı 17.1 (V m/A) olarak ölçüldü. Yükseltme faktörü 20 olarak elde edildi. Maksimum çizgisellikten sapma bu sistem için %15.3 olarak hesaplandı. İkinci düzenekte ise iki yükseltici seri bağlı ve bu yükselticilerin isimleri AD600 ve AU-1291'dir. Bu sistemin duyarlılığı 5.45 (V m/A) olarak ölçüldü. Maksimum çizgisellikten sapma %2.7 olarak hesaplandı. Seri bağlı yükselticilerin varlığı yükseltme faktörünü 160000'e çıkardığı için ikinci sistem tercih edildi. Mevcut ekipman ile en yüksek duyarlılığa sahip bobin sarılmış olsa da performans yine de yetersiz kaldı ve daha yüksek duyarlılığın gerekli olduğu sonucuna varıldı. Geliştirilmiş olan yazılım ile ümit verici başka bobinler dizayn edildi, ancak bunlar sarılmadı. Yine de performansın etki yaratacak kadar artması beklenmemektedir. 10^7 'ye varan bir duyarlılık oranı, yükselticinin ayarlanması ile aşılması mümkün olmayan bir güçlük teşkil etmektedir, çünkü sinyal gürültü oranında iyileşme gözlenmemekte ve ölçülmek istenen sinyal gürültü seviyesinin altında kalmaktadır. Ancak bir durum için optimum bobin değişkenlerini veren yazılım birden fazla uygulama için yararlı olabilmektedir. Ayrıca bu yazılım dikdörtgen bobin, düz-spiral bobin gibi farklı bobin türlerini optimize etmek üzere modifiye edilebilir, böylece olası sensör dizaynlarının yelpazesinin geniş tutulmasına olanak sağlanabilir. Sistemin duyarlılığı ve çizgiselliği analiz edildi. LAEET'in yanısıra, manyetik sensörlerin kablosuz güç aktarımı uygulaması da araştırıldı. Güç aktarımı verimliliğini maksimize eden koşullar incelendi. Güç aktarımında verimliliğin en önemli koşulu olan optimum kalite faktörüne sahip bobini bulmak için maksimum duyarlılığı veren bobin boyut değişkenlerini elde etmemizi sağlayan algoritma burada da kullanıldı. Dört bobinli kablosuz güç aktarımı sistemi seçildi, dizayn edildi ve uygulamaya geçirilerek analitik sonuçlarla karşılaştırma yapıldı. Dizayn edilen sistemin verimliliği %7.6 olarak ölçüldü. Bu değer, sarımlarda enamel bakır tel yerine litz teli kullanılmak suretiyle %39'a yükseltildi.

Anahtar Kelimeler: Manyetik Alan Sensörleri, Biyomedikal Uygulamaları, LAEET, Lorentz Alanı, Endüksiyon Bobini, Bobin Dizaynı

My mother and father, I will love you forever

ACKNOWLEDGMENTS

I would like to express my gratitude to Prof. Dr. Nevzat G. GENÇER for his support, guidance and patience through this study. He did not stop believing in me even after all the misfortune I have been through. As I applied the improvements he suggested, I understood the value of his guidance. I also got a head start thanks to the resources he provided. I would like to thank Mürsel KARADAŞ for his contributions to the experimental work of this study, since one of the applications included a collaborative study with him. I would like to thank Dr. Reyhan (TUTUK) ZENGİN for her always helpful attitude, and also Dr. Balkar ERDOĞAN for his support and advices through this study. Finally I want to thank my mother Canan İNAN for all of her emotional support and patience.

TABLE OF CONTENTS

ABSTRACT	v
ÖZ	vii
ACKNOWLEDGMENTS	x
TABLE OF CONTENTS	xi
LIST OF TABLES	xiv
LIST OF FIGURES	xv
CHAPTERS	
1 INTRODUCTION	1
1.1 Magnetic Sensors	1
1.2 Induction Coil Sensors	3
1.3 Air-Cored Induction Coil in Biomedical Applications	7
1.4 Objectives of the Thesis	11
1.5 Outline of the Thesis	11
2 THEORY	13
2.1 Introduction	13
2.2 Formulation for Induced Voltage on an Air Cored Induction Coil	13
2.2.1 Multilayer Coil	14

2.2.2	Flat Spiral Coil	16
2.3	Formulation for Induced Voltage on an Air Cored Induction Coil	17
2.3.1	Parallel Resonant Circuit	20
2.3.2	Series Resonant Circuit	21
2.3.3	Frequency Response Comparison of Parallel and Series Resonant Circuit	22
2.4	Frequency Related Parameters	24
2.4.1	K Parameter	25
2.4.2	Inductance Parameter	27
2.4.3	Capacitance Parameter	28
2.5	Magnetic Field Produced by an Induction Coil	30
3	DESIGN OF THE MAGNETIC SENSOR	35
3.1	Introduction	35
3.2	The Effect of Coil Parameters	35
3.2.1	Coil Diameter	36
3.2.2	Coil Length	37
3.2.3	Wire Diameter	37
3.3	Coil Parameter Optimization	37
3.4	Amplifier Design	40
3.5	Frequency Response of the System and Noise Analysis	43
4	EXPERIMENTAL WORK	47
4.1	Introduction	47
4.2	Test of the Induction Coil Design	47

4.3	LFEIT Application	55
4.4	Wireless Power Transfer (WPT) Application	65
5	CONCLUSION AND DISCUSSION	79
	REFERENCES	83

LIST OF TABLES

TABLES

Table 1.1 Magnitude and frequency range of different magnetometers	3
Table 4.1 Comparison of theoretical and measured inductance/resistance values for different coils.	50
Table 4.2 Comparison of the theoretical and experimental capacitance values and resonance frequencies for different coils.	50
Table 4.3 Measured and calculated voltage output for different magnetic field input at respective measurement distances	51
Table 4.4 Measured and calculated voltage outputs after modification of inductance by including mutual inductances and respective coupling coefficient value measurements	53
Table 4.5 Measured voltage outputs at two different frequencies of importance for a range of measurement distance and respective coupling coefficient values	63
Table 4.6 Size parameters of the coils with optimum quality factor	72
Table 4.7 Critical parameters of the coils modified to include Litz wires as their windings	77
Table 4.8 Critical parameters of the secondary coil modified further to have high loaded quality factor	77

LIST OF FIGURES

FIGURES

Figure 1.1	Types of Magnetometers	2
Figure 1.2	Air-cored induction coil (Disk coil) a) Side view, b) Top view	4
Figure 1.3	Air-cored induction coil (Rectangular multilayer coil) a) Side view, b) Top view	5
Figure 1.4	Induction coil (Disk coil) with ferromagnetic core	5
Figure 1.5	Spiral Planar coil a) Top view, b) Side view	6
Figure 1.6	The main configuration of the system	7
Figure 1.7	The electrical signal detected by the measurement electrodes and its relation with conductivity gradient	9
Figure 1.8	Sketch of the WPT system	11
Figure 2.1	Coil parameters for multilayer coil	15
Figure 2.2	Packing Factors of Two Different Winding Configurations	16
Figure 2.3	Coil parameters for flat spiral coil	17
Figure 2.4	α Representing the Angle Between Sensor Coil and Magnetic Field (B)	18
Figure 2.5	The Equivalent Circuit of Three Different Configurations	19
Figure 2.6	Induction Coil Connected to a Voltage Amplifier	21

Figure 2.7 Induction Coil Connected to a Current Amplifier	23
Figure 2.8 Comparison between the Frequency Responses of Parallel Resonance and Series Resonance Configurations. Results are obtained for 1 nT input and an amplification factor of 20. The parallel resistance R_{II} is 100 Ω	24
Figure 2.9 Magnetic Field on the Axis of a Current Loop	32
Figure 2.10 Magnetic Field on the Axis of a Multilayer Air-Core Solenoid	33
Figure 2.11 Magnetic Field on the Axis of an Induction Coil vs position	33
Figure 3.1 Output voltage versus coil diameter for different coil lengths	36
Figure 3.2 The effect of coil length	38
Figure 3.3 Wire diameter vs output voltage for different coil diameter and length combinations	39
Figure 3.4 Optimization GUI Software	41
Figure 3.5 Improved optimization GUI software example 1	41
Figure 3.6 Improved optimization GUI software example 2	42
Figure 3.7 Transient analysis of amplifier circuitry. Simulation software used is multisim. Green signal is the input of the amplifier, indicated as V_6 . Red signal is the output of the amplifier, indicated as V_1 . The operating frequency used in the simulation is 2.2 MHz	43
Figure 3.8 Noise equivalent circuit [10]. $\frac{U_R^2}{\Delta f}$ and $\frac{i_R^2}{\Delta f}$ are the noise voltage representing the thermal noise of the coil resistance R and the noise current representing the damping resistor R_{II} respectively. $\frac{U^2}{\Delta f}$ and $\frac{I_R^2}{\Delta f}$ represent the internal noise voltage and internal noise current of the amplifier	45

Figure 3.9 Signal, noise and magnetic noise comparison for the first system designed for LFEIT application. Simulation software used is MATLAB. Input magnetic flux density is 1 nT. Amplifier used is AD797. Parallel resistance R_{II} is 100 Ω	46
Figure 4.1 Transmitter coil circuit. Signal given from function generator is measured on 1.2 k Ω resistance in order to determine the current through the transmitter coil later to be used in (2.47) to calculate the input magnetic field of the sensor.	49
Figure 4.2 Receiver stage. Low noise high input impedance amplifier AD 797 is used.	52
Figure 4.3 Comparison of the theoretical and measured output voltages for a range of magnetic flux density values (on the order of nT) as given in Table 4.3. The operation frequency is 2.8 MHz.	52
Figure 4.4 Data obtained through measurement and its linear approximation .	54
Figure 4.5 Experiment setup without test tube, sensor and ultrasound input, the width of the mid section is greater than the diameter of the test tube and 2.5 cm [15]	56
Figure 4.6 Optimum coil designed for LFEIT application (20 mm coil diameter, 2.5 mm coil height (length), 0.6 mm wire diameter) a) Top view, b) Side view	57
Figure 4.7 Simulation results for the amplifier circuitry designed for LFEIT application. The left hand side shows the input signal characteristics(20 uV, 1 MHz). On the right hand side, the output signal is observed at channel B. The amplification can be calculated as 40mV/20uV=2000. Input signal (channel A) is too small to be revealed on the oscilloscope screen. .	58

Figure 4.8 Simulation results for the amplifier circuitry designed for LFEIT application(second AD600 excluded). The left hand side shows the input signal characteristics (20 uV, 1 MHz). On the right hand side, the output signal is observed at channel B. The amplification can be calculated as $2.25/20\text{mV}=112.5$. Input signal (channel A) is also shown on the oscilloscope screen and it is 20 mV in amplitude.	59
Figure 4.9 Amplifier circuitry designed for LFEIT application	59
Figure 4.10 The detailed schematic of the first stage of the amplifier circuit . . .	60
Figure 4.11 Pin configuration and internal structure of AD600	60
Figure 4.12 The amplifier circuit board	61
Figure 4.13 GUI results for LFEIT application (with 10 pT input and maximum coil and wire diameter constraints)	61
Figure 4.14 Data obtained through measurement and its linear approximation . .	64
Figure 4.15 GUI results for LFEIT application with 0.1 pT input and maximum coil diameter and wire diameter constraints of 2 cm and 0.6 mm respectively. Operation frequency is 1 MHz. Output voltage is calculated as 0.37 mV. Optimum coil length is computed as 2.5 mm. Wire diameter of the optimized coil is 0.6 mm.	64
Figure 4.16 GUI results for LFEIT application with 6 mm wire diameter constraint. This value is chosen high enough to check whether there is a better coil if there were no wire diameter constraint. Output voltage for the determined optimum coil is calculated as 0.7 mV. Wire diameter is computed as 1.57 mm. Optimum coil length is also changed and it is 2 cm.	65

Figure 4.17 Improved GUI results for LFEIT application with 0.6 mm wire diameter constraint. Improved GUI includes additional software that determines whether flat spiral coil or air-cored multilayer coil performs better. It is observed that a flat spiral coil provides a slightly better output voltage (0.4 mV) compared to the results given in Figure 4.15. Since the optimum coil type is determined as flat spiral, instead of coil length parameter, the turn spacing parameter is included. Wire diameter of the optimum coil is calculated as 0.2 mm and the turn spacing is 0.004 mm. 66

Figure 4.18 Improved GUI results for LFEIT application with 6 mm wire diameter constraint. The results are same as in Figure 4.16 since the optimum coil type for this case is air-cored multilayer coil. 66

Figure 4.19 The schematic of the final version of the experiment setup. Dc magnetic field is seen at inward direction which is perpendicular to the measurement axis. Induction coil sensor is placed adjacent to the tube in order to obtain best sensitivity performance. 67

Figure 4.20 The illustration of expected results of the experiment. The scale among the signals to be measured is represented in this figure. The signals with greater amplitude correspond to outer boundaries with higher conductivity gradient namely the boundary between air and oil, salt water and tube respectively. These expected signals are out of phase 180 degrees. The waveform in the middle corresponds to the conductivity gradient between salt water and oil therefore it is smaller. The aim is to observe this smaller signal since it will prove whether the conductivity difference between two different tissues can be distinguished. 68

Figure 4.21 The illustration of results of the experiment. The outer boundary signals are obtained at a scale of 5 V. However the noise signal obtained is greater than the expected inner boundary waveform, therefore it was not possible to distinguish this signal from the noise. 69

Figure 4.22 Theoretical results for noise analysis of the experiment setup for 0.1 pT input magnetic flux density. It is observed that the output voltage of the sensor is below the noise level. 69

Figure 4.23 Theoretical results for noise analysis of the experiment setup for 10 pT input magnetic flux density. This simulation indicates that if it is possible to increase the input flux density by using a higher magnitude DC field or placing the sensor closer to the source with a different configuration, output signal reaches above the noise level at the resonance frequency. 70

Figure 4.24 Four coil wireless power transfer system. In the figure, k_{mn} is the coupling factor between coil m and coil n, and Q_m is the quality factor of coil m 71

Figure 4.25 Four coil wireless power transfer system circuitry schematic including components with their respective values 73

Figure 4.26 Optimum quality factor coil designed for WPT application (30 mm coil diameter, 5 mm coil height(length), 1 mm wire diameter) a) Top view, b) Side view 74

Figure 4.27 Optimum quality factor coil with litz wire windings designed for WPT application (30 mm coil diameter, 5 mm coil height(length), 1 mm wire diameter) a) Top view, b) Side view 76

CHAPTER 1

INTRODUCTION

1.1 Magnetic Sensors

Magnetic sensor is a device that measures the magnetic field in a medium. The range of frequencies and magnitudes of these fields are very wide. Therefore different types of magnetic sensors are required for their measurement. As shown in Figure 1.1, the magnetic field sensors are divided into two: The ones measuring the magnitude of the field and the ones measuring the vector component of the field. The types measuring vector component are also divided into two sections: Magnetometers, which are specialized in measuring low magnetic fields ($< 1mT$) and gaussmeters, which are specialized in measuring high magnetic fields ($> 1mT$).

The most recent of the magnetometers is fiber optic magnetometer. Various optical techniques are used in these devices. One of these is the magneto-optic Kerr effect (MOKE) [1]. In this technique, the sample surface is exposed to light which has a nonlinear interaction with the surface causing the reflected light to have an elliptical polarization and that is measured by a detector. It is still in development and its performance is as good as fluxgate magnetometers currently. The superconducting quantum interference device (SQUID) has the highest sensitivity among magnetometers [2]. These sensors need an ambient temperature about $0^{\circ}K$, therefore it is highly dependent on external conditions. These devices are more expensive than other magnetometers. They are usually used to measure biomagnetic signals due to its high sensitivity and flat noise spectrum around frequency range of interest [3].

The Hall effect device is the most common magnetic field sensor used in gaussmeters,

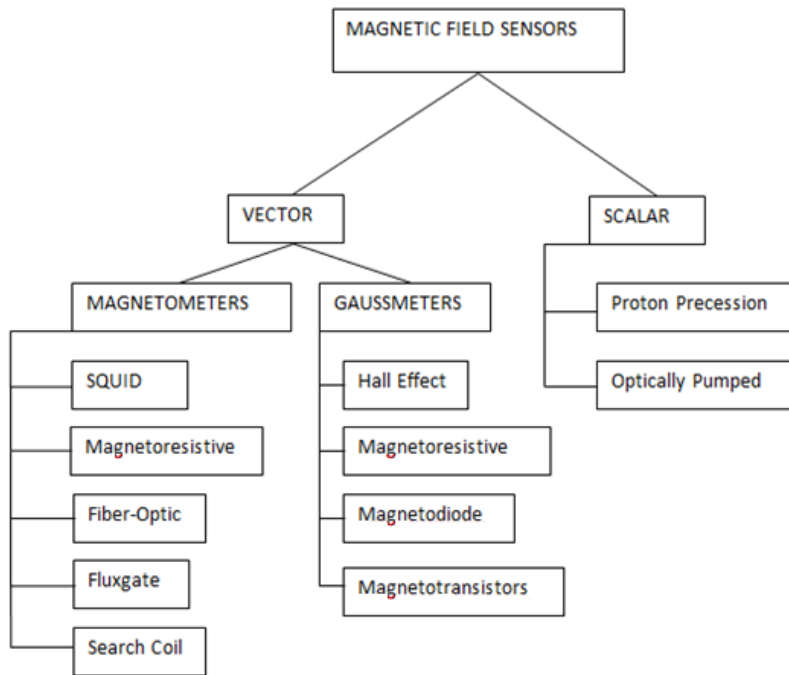


Figure 1.1: Types of Magnetometers

that is designed to measure very high fields ($> 1T$) [4]. Its basic principle is varying its output voltage due to the change in the input magnetic field. Therefore it can be used in switches, current sensors, position sensors, etc [5].

The magneto-resistive sensors are both used in gaussmeter and magnetometer applications due to their wide range of operating magnetic field strengths ($10^{-3} - 10$ mT). Anisotropic magnetoresistors (AMR) are used in magnetometers for some applications. The giant magneto-resistive effect (GMR) provides better sensitivity and may be used instead of fluxgate magnetometers in some of the applications [6], [7]. The proton precession magnetometer is the most widely used device to measure only the strength of the magnetic field. Its principle is related to the atomic constants; therefore it is also used for calibration purposes. The optically pumped magnetometer operates slightly better than proton precession magnetometer but it is more expensive. The fluxgate magnetometer is composed of a ring shaped core with high magnetic permeability and two windings wound around it. One of the windings is for driving and the other is for sensing. AC current is introduced to the driving winding, causing the magnetic saturation of the core to alternate. This alternating magnetic field causes an

induced

Table 1.1: Magnitude and frequency range of different magnetometers

Instrument	Range (mT)	Resolution (nT)	Bandwidth (Hz)
Induction Coil	10^{-10} to 10^6	Variable	10^{-1} to 10^6
Fluxgate	10^{-4} to 0.5	0.1	dc to 2×10^3
SQUID	10^{-9} to 0.1	10^{-4}	dc to 5
Hall effect	0.1 to 3×10^4	100	dc to 10^8
Magnetoresistance	10^{-3} to 5	10	dc to 10^7
Proton precession	0.02 to 0.1	0.05	dc to 2
Optically pumped	0.01 to 0.1	0.005	dc to 5

voltage, which is picked up by sensor windings. Fluxgate magnetic sensors are widely used, high performance, not expensive sensors. Another magnetic sensor with high performance and low cost is induction coil (search coil) magnetometer [8]. Induction coil magnetometer is based on Faraday's Law. Induction coil magnetometer sensitivity and resolution are variable and can be adjusted; therefore it can be used in a great variety of applications. It cannot measure DC magnetic fields or very slowly varying magnetic fields. Table 1.1 illustrates the magnitude and frequency range of the sensors mentioned above [9].

1.2 Induction Coil Sensors

Induction coil sensor [10], [11] is a magnetic field sensor whose working principle is based on Faraday's law of induction. The description of the coil sensor was given in 1960s [12]. In time, the coil sensors have become more popular and used in various applications such as proximity sensors, traffic light sensors, metal detection, biomagnetic measurements. There are mainly two types of induction coil sensors: Air-cored and ferromagnetic core coil types. First one does not have core material. On the other hand, ferromagnetic core coil has soft magnetic material as core such as silicon iron or mu-metal. The coils are classified by their shapes according to the applications they are used in. An air-cored disk coil side view is shown in (Figure 1.2a) and top view in (Figure 1.2b). A disk coil with ferromagnetic core is illustrated in (Fig-

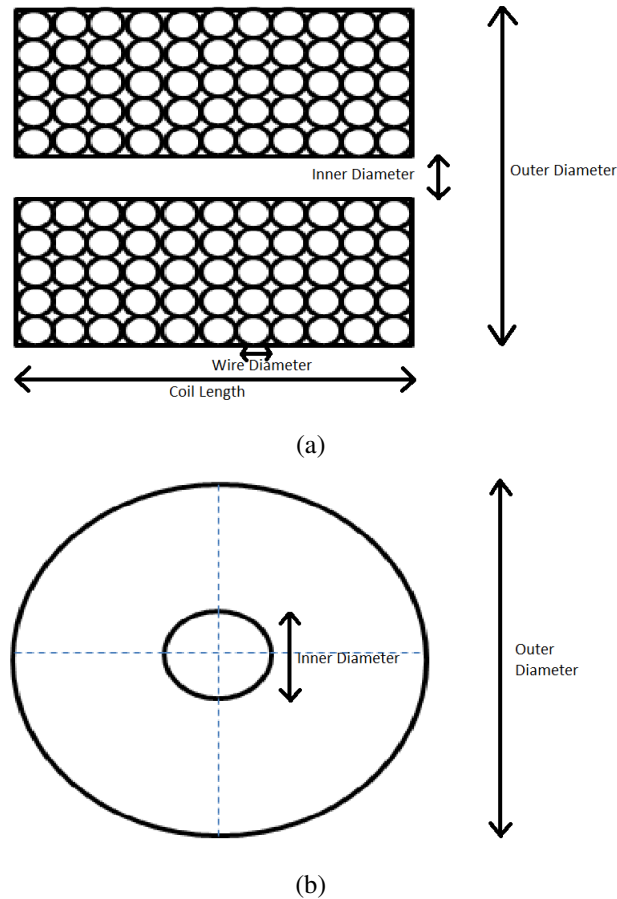


Figure 1.2: Air-cored induction coil (Disk coil) a) Side view, b) Top view

ure 1.4). Instead of a disk coil, a rectangular multilayer coil is sometimes preferred (Figure 1.3a, Figure 1.3b). A spiral planar coil is shown in (Figure 1.5a, Figure 1.5b).

The air coil sensor has lower sensitivity, especially when it is small in size. The relative magnetic permeability introduced by the ferromagnetic core element increases the sensitivity greatly. Let us consider a search coil sensor with high sensitivity, including an amorphous ribbon (Metglas 2714AF) core which is described in [13]. Its sensitivity is measured to be about 300 times larger in comparison with an air coil sensor with the same dimensions [8]. The ferromagnetic core coils has increased sensitivity compared to air-cored coils of same dimensions. However this increase in the sensitivity costs one of the most important features of air-cored coil, which is linearity. Even the best ferromagnetic material core performs poorly in terms of linearity since many non-linear factors including temperature, frequency, flux den-

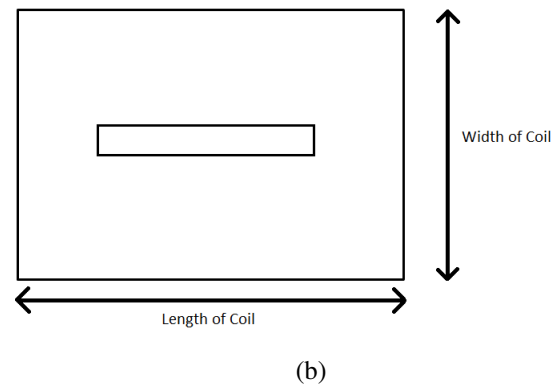
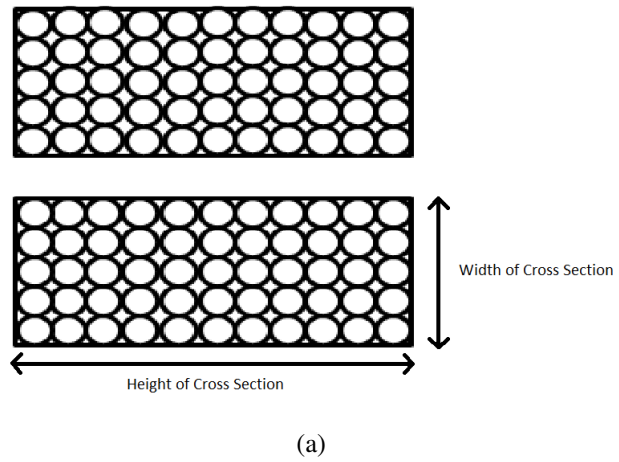


Figure 1.3: Air-cored induction coil (Rectangular multilayer coil) a) Side view, b) Top view

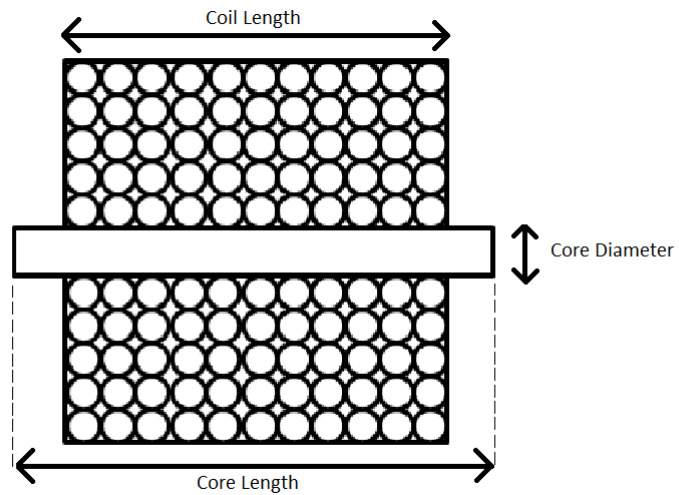
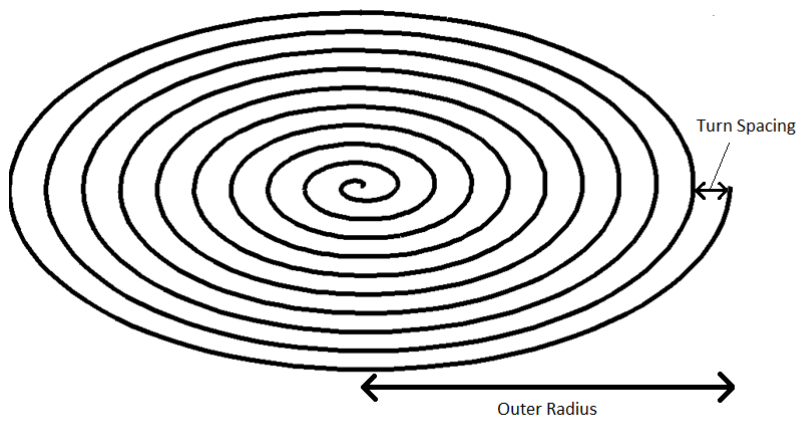
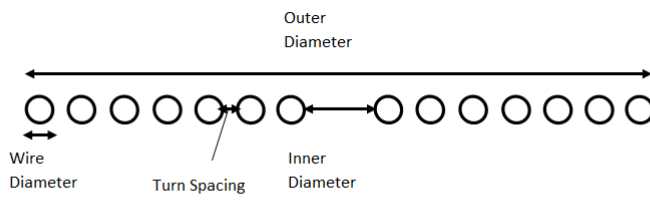


Figure 1.4: Induction coil (Disk coil) with ferromagnetic core



(a)



(b)

Figure 1.5: Spiral Planar coil a) Top view, b) Side view

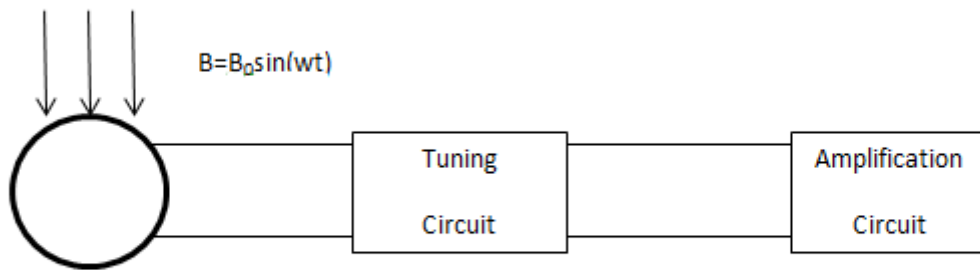


Figure 1.6: The main configuration of the system

sity etc. are introduced by core to the transfer function of the sensor. Besides, the use of ferromagnetic core increases the noise (e.g. Barkhausen noise), which further decreases the sensor's output performance. Another very important hindrance is the disturbance in the magnetic field to be measured, caused by the ferromagnetic core.

Due to the problems mentioned above and the strong requirement of linearity for biomedical applications of magnetic sensors, air-cored induction coil sensor is preferred over others. These applications require measurement of magnetic fields of specific range and frequency. The coil and the amplification stage are to be designed accordingly.

1.3 Air-Cored Induction Coil in Biomedical Applications

The applications of air-cored induction coil in biomedical area are challenging due to the reasons such as the magnetic field to be measured having relatively high frequency (kHz-MHz range) or low magnitude (pT range). Therefore a specific coil design combined with amplifier circuitry is required for each application. The main configuration of the system (Figure 1.6) also includes a tuning circuit part which tunes the circuit to the resonance frequency.

Biomedical applications of air-cored induction coils include Magnetic Induction To-

mography (MIT), Contactless conductivity imaging, Lorentz field electrical impedance tomography (LFEIT), wireless power transmission, etc.

One of the applications that will be investigated through this study is Lorentz force electrical impedance tomography (LFEIT) [14], [15]. Tissues in the body have different conductivities. The contrast between neighboring tissues allow them to be distinguished by conductivity. LFEIT is a technique of Electrical impedance tomography (EIT) method to measure the conductivity of different tissues which is then used for imaging purposes [16]. EIT method includes electrodes being placed around the body or the organ of interest. Then by injecting electrical current through one of the electrodes and measuring its distribution through tissues with the others, electrical impedance properties of different areas are obtained. This information then leads to an image reconstruction process. This technique has a weakness that is the low spatial resolution due to positional problems [17]. In order to increase the spatial resolution for this technique which can image the body through a specific property, improvements are sought. It is observed that causing vibration inside a magnetic field using ultrasound waves, induces a current proportional to the electrical conductivity of the conductor by Lorentz force [18]. This method is called LFEIT. Its alternative names are: Magneto-Acousto-Electrical-Tomography [19] or scan of electric conductivity gradients with ultrasonically induced Lorentz force [20]. The advantage of LFEIT is that its spatial resolution is close to ultrasound imaging applications. The disadvantage however is the magnitude of induced current being very small. Thus a very sensitive induction coil with good signal-to-noise ratio (SNR) is required to obtain this current. An illustration of the expected signal is given in Figure 1.7. As observed from this figure, in order to obtain the electrical signal, a change in the conductivity, leading to a conductivity gradient is required. The phase of this signal depends on the sign of the conductivity gradient. The illustration also shows that the magnitude and phase of the electrical signal obtained is proportional to the convolution product of conductivity gradients and the ultrasound pressure wave [16]. Therefore the signal strength is proportional to the difference of conductivity between two neighboring medium. This difference is high at the boundary between tissues. Detecting the signal at these locations are the main objective. A very high quality current sensor is required to achieve this.

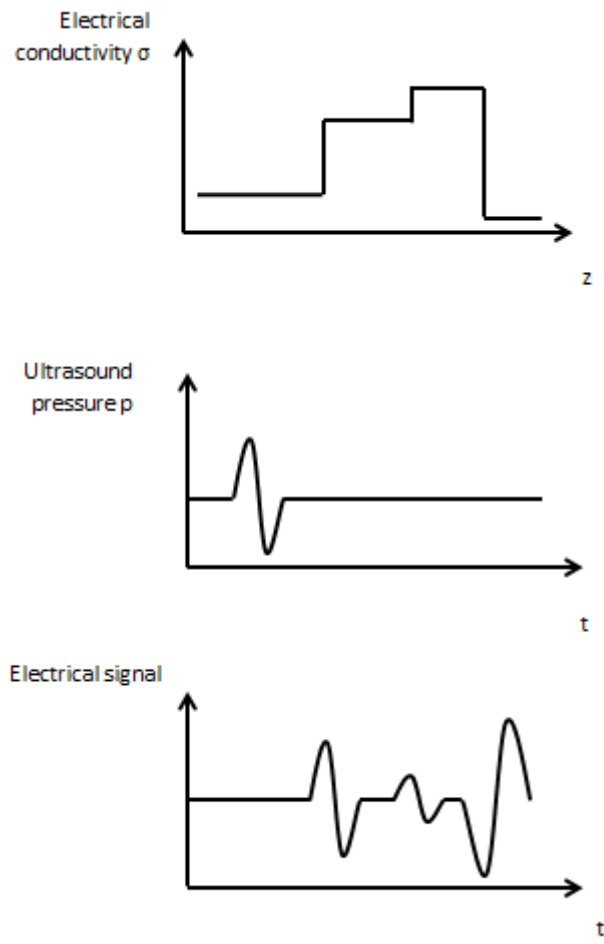


Figure 1.7: The electrical signal detected by the measurement electrodes and its relation with conductivity gradient

Another biomedical application of air-cored induction coil is wireless power transfer [21]. The charging through wireless induction with ferromagnetic core should be avoided due to core increasing the size of the device as well as posing danger of interacting with its environment. These environments include wet and chemical medium such as humid air or human body. Therefore it is possible to implement wireless power transfer with air core induction in biomedical systems [22], [23]. Secondary coil implanted inside the human body can be powered by the external primary coil, providing power for the device. The advantage of this is the disappearance of the need for invasive methods such as changing a battery inside of a body or placing wires to charge the battery.

Wireless power transfer (WPT) applications may require various types of coils according to the device it is implemented in. In [21], a multilayer coil is designed to resonate at 125 kHz operating frequency whereas in [24], a chain of coils are used all tuned to 7.65 MHz in order to transfer power more efficiently. The choice of type and size of coil depends on the conditions providing the maximum power transfer at the operating frequency. The system includes a single loop driving coil, transmitter (Tx) coil, receiver (Rx) coil and another loop (Load loop) between the Rx coil and load. The sketch of the system is given in Figure 1.8. Both transmitter and receiver parts are to be designed in order to obtain an optimum result. In order to maximize power transfer, transmitter and receiver parts should be in resonance. So in addition to other magnetic sensor applications where adjusting the transmitter part is enough, the receiver part should also be tuned in wireless power transfer applications. LFEIT application of induction coil sensor did not require this, because it is a current sensing application where the magnetic field is obtained in order to sense the current causing it. In WPT applications however, the goal is to sense the magnetic field itself, therefore generation of the magnetic field to be sensed is also adjusted according to the specific application. Due to the need for induction coil sensors to be used in applications with various specifications, a flexible design is required to cover a wide range of operating frequency and include some size related constraints. This design should also check the different coil types given in the previous section(multilayer coil, flat spiral coil) for their advantages.

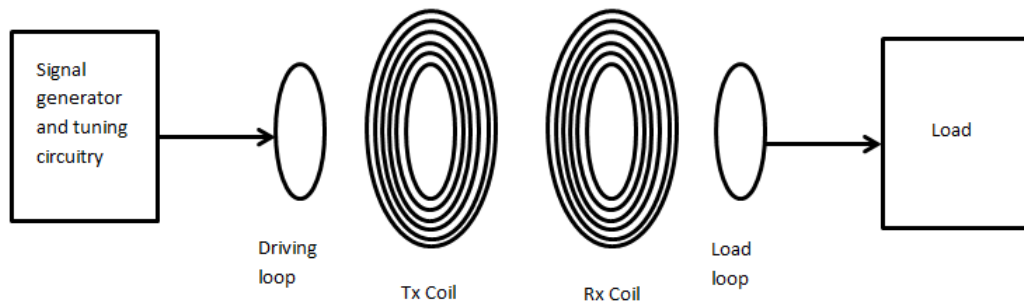


Figure 1.8: Sketch of the WPT system

1.4 Objectives of the Thesis

The objectives of the thesis are listed below:

- To design an air-cored induction coil with best sensitivity for various cases in biomedical applications. A software should be developed to specify the geometry of the coil that gives the optimum performance for a specific application.
- To perform experiments to verify the design in detail in order to be able to use it in different applications.
- To implement certain biomedical applications and to determine the performance of the sensors including amplifiers.

1.5 Outline of the Thesis

Chapter 1 is an introduction on magnetic sensor types, induction coils, and biomedical applications of interest. In Chapter 2, the theory of designing an induction coil, its important parameters and the relationship between them are given. Afterwards in

Chapter 3, the formulations given in Chapter 2 are used in order to develop an optimization software whose mechanism is explained in detail. Chapter 4 includes all the experimental work done for both verification and implementation of the design. Chapter 5 concludes with discussion of the performance of the design and the results of the applications.

CHAPTER 2

THEORY

2.1 Introduction

The measurement of magnetic fields of high frequency and low magnitude requires careful design of the sensor coil and the amplification circuitry. The main challenges that need to be overcome are the tuning of the circuit to the resonance frequency and designing a low noise amplifier stage. The maximum sensitivity is needed at high frequency (kHz-MHz). There are also challenges caused by the specific application that the magnetic sensor is desired to use. These are usually caused by the system restrictions affecting the sensor geometry or small source of magnetic field.

Firstly, formulations related to output voltage of an air cored induction coil due to an AC magnetic field, including coil parameters will be given. Frequency response with additional amplifier circuitry and tuning methods will be observed. Then the different coil types and their frequency related parameters will be investigated. Finally, the magnetic field produced by an induction coil as a function of distance will be studied.

2.2 Formulation for Induced Voltage on an Air Cored Induction Coil

Formulations differ among the types of air cored induction coils, therefore there will be two subsections related to each type: Multilayer coil and flat spiral coil.

2.2.1 Multilayer Coil

As stated by the Faraday's Law, the voltage output U of an induction coil with n turns is calculated according to the formula below:

$$U = -n \frac{d\phi}{dt} \quad (2.1)$$

where n is the turn number and ϕ is the time varying magnetic flux through each turn. For a sinusoidal flux variation:

$$\phi = \phi_{max} \cos(\omega t) \quad (2.2)$$

where ω is the angular frequency. Combining (2.2) with (2.1), voltage induced on the coil takes the following form:

$$U = n\omega\phi_{max} \sin(\omega t) \quad (2.3)$$

The magnitude of the resulting signal is:

$$U_0 = n\omega\phi_{max} \quad (2.4)$$

where U_0 is the open-loop peak value of the coil output voltage. The turn number n depends on the size parameters of the coil and diameter of the wound wire. These parameters are shown in Figure 2.1. The formulation relating the turn number to the coil size and wire size is:

$$n = l \frac{D - D_i}{2kd^2} \quad (2.5)$$

k is called the packing factor, which is a constant determined by the winding style, usually around 0.8-0.9. It can be obtained by dividing the total wire cross-sectional area to the winding cross sectional area. Obtaining the packing factor is illustrated in Figure 2.2 by illustrating two extreme cases. In the experiments, this factor is calculated by the ratio of real turn number to the turn number according to Equation

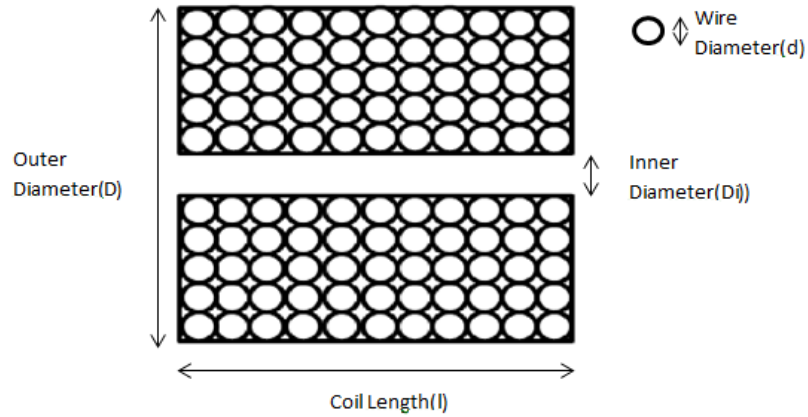


Figure 2.1: Coil parameters for multilayer coil

(2.5) since the coils of our interest are wound by hand. This turn number determined by Equation (2.5) is the maximum turn number that can be wound on a designed coil. However the coil may not be fully wound, resulting in less turn number. This may be useful for tuning the coil, however it will decrease the sensitivity and the applications of interest usually require high sensitivity. Therefore winding the coil with the maximum turn number will be necessary.

ϕ_{max} is the peak value of the magnetic flux through single turn. Magnetic flux depends on flux density, sensor coil area and the angle between coil and input magnetic field. This angle is illustrated in Figure 2.4. In order to maximize the measurement signal, ϕ_{max} can be expanded as:

$$\phi_{max} = B_{max} S \cos\alpha \quad (2.6)$$

where S is the sensor coil area. Therefore combining equations (2.1) to (2.6), the induced voltage on the multilayer sensor coil in terms of coil parameters is:

$$U_0 = \frac{1}{2} \pi^2 f l \frac{D - D_i}{2kd^2} F B_{max} \frac{(D + D_i)^2}{4} \cos\alpha \quad (2.7)$$

where F is the transfer function which depends on the operating frequency and the

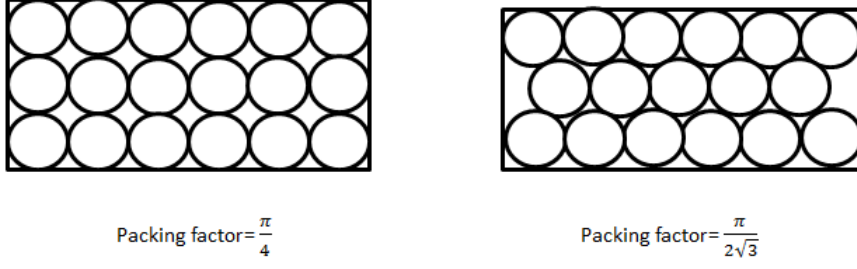


Figure 2.2: Packing Factors of Two Different Winding Configurations

resonance frequency. This term is related to the tuning of the circuit and therefore will be explained in detail in the next section (section 2.3).

2.2.2 Flat Spiral Coil

The formulations (2.1) to (2.4) are also valid for flat spiral coil. However the relation of turn number to coil geometry differs for this case. Instead of (2.5), for a flat spiral coil, the equation for turn number becomes:

$$n = \frac{D - D_i}{2(d + s)} \quad (2.8)$$

where D is the outer spiral diameter, D_i is the inner spiral diameter, d is the wire diameter and s is the spacing between two turns all in meters. These parameters are illustrated in Figure 2.3. Another difference from equation (2.5) is the absence of packing factor k since the spiral coil is loosely wound for most of the applications. Therefore a more general equation for induced voltage on the sensor coil:

$$U_0 = \frac{1}{2} \pi^2 f n F B_{max} \frac{(D + D_i)^2}{4} \cos \alpha \quad (2.9)$$

where n is obtained using (2.5) for multilayer coil and (2.8) for flat spiral coil.

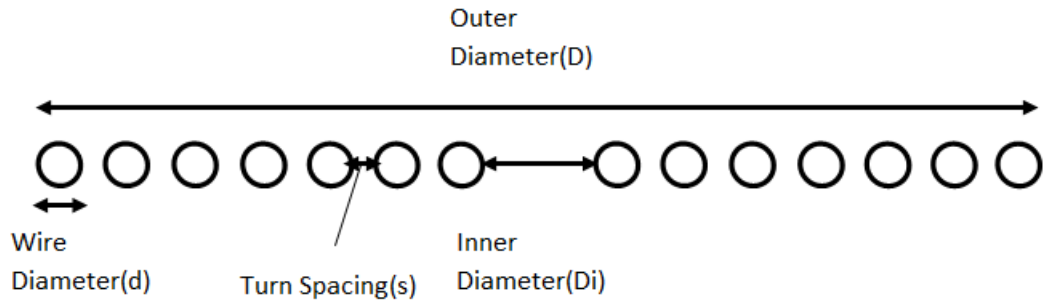


Figure 2.3: Coil parameters for flat spiral coil

2.3 Formulation for Induced Voltage on an Air Cored Induction Coil

There are three common configurations of coil circuits: Series resonant circuit (Figure 2.4(a)), parallel resonant circuit (Figure 2.4(b)) and transformer coupled circuit (Figure 2.4(c)). The series resonant circuit, at the resonance frequency, draws maximum current due to the minimized impedance. On the other hand, parallel resonant circuit has maximum impedance; therefore the output voltage is maximized. Even though the resonant current is minimum, the current circulating around the coil loops is strong. The series resonant circuit should be connected to a low input impedance (current) amplifier. Other configurations are to be connected to a high input impedance (voltage) amplifier.

Figure 2.4 shows the equivalent circuit of air-cored induction coil. The coil inductance L , coil resistance R , series capacitance C_s , parallel capacitance C_p , tuning capacitance C_{II} are the parameters of interest. These parameters are to be determined as accurate as possible to design the amplifier properly. The capacitance and induc-

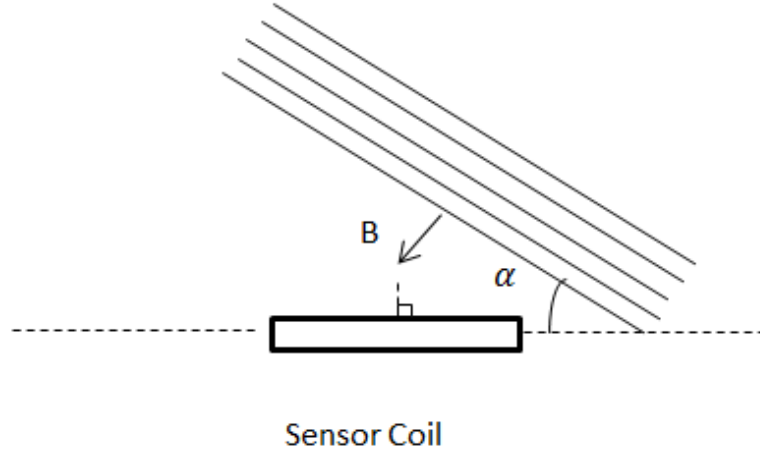


Figure 2.4: α Representing the Angle Between Sensor Coil and Magnetic Field (B)

tance of the coil are the main parameters that affect the resonance frequency. They are mainly determined by the coil geometry and wire size. The methods to determine these parameters will be given in detail in the next section of this chapter.

The impedance of a coil is defined in terms of the effective inductance L , the frequency f and the tangent of the phase angle denoted by Q . This value is called the *quality factor* of the coil at the resonant frequency. For all frequencies, Q can be modified as:

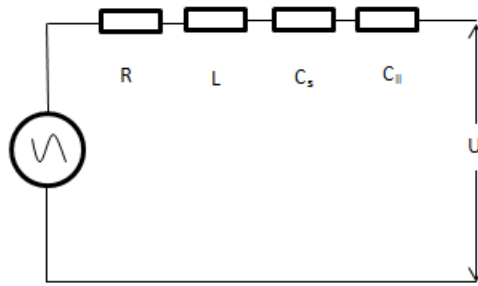
$$Q' = Q(1 - \omega^2 LC) \quad (2.10)$$

When $\omega^2 LC$ term is equal to 1, Q' is equal to 0. Therefore the frequency where:

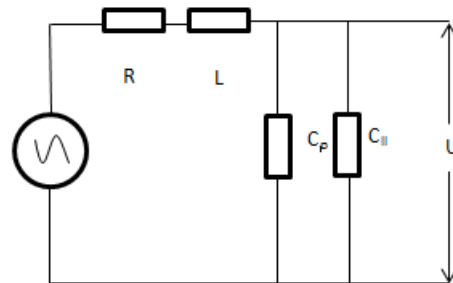
$$\omega_0 = \frac{1}{\sqrt{LC}} \quad (2.11)$$

is called the *self resonant frequency* [25].

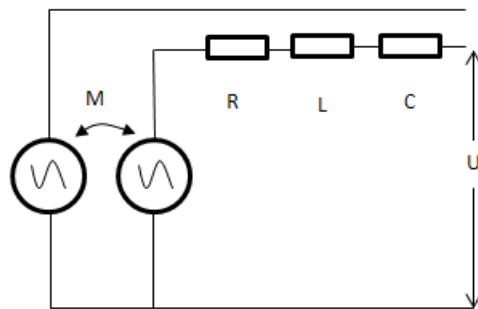
The frequency response of the circuit depends not only on the coil but also on the circuit configurations. Figure 2.5 shows equivalent circuits for three different configurations. Although in the figure, three configurations are shown, the transformer



(a) *Series Resonant Circuit*



(b) *Parallel Resonant Circuit*



(c) *Transformer Coupled Circuit*

Figure 2.5: The Equivalent Circuit of Three Different Configurations

coupled circuit is also considered as parallel resonant type, therefore the main focus will be on the comparison between the series and parallel resonant circuits.

2.3.1 Parallel Resonant Circuit

The parallel resonant circuit is to be connected to a high input impedance amplifier stage. This is also called voltage amplifier. The schematic of the circuit including a basic voltage amplifier stage is shown in Figure 2.6. R_i is the input impedance of the amplifier, C_i is the input capacitance of the amplifier and R_{II} is the external resistance for further adjusting the damping of the circuit. C_{II} is the total parallel capacitance seen on the coil. The contributions to this component are from the coil and the external capacitance used for tuning. Output voltage of the circuit with respect to angular frequency, using the expression from (2.7) is:

$$U_A(w) = AV_0(w) \quad (2.12)$$

where A is the amplification factor, V_0 is the output voltage of coil and the transfer function $F(w)$ from (2.7) can be expressed as:

$$F(w) = \frac{K}{1 - \left(\frac{w}{w_r}\right)^2 + i2D\frac{w}{w_r}} \quad (2.13)$$

where K is a voltage division factor:

$$K = \frac{R_{II}}{R + R_{II}} \quad (2.14)$$

and w_r is the resonant angular frequency

$$w_r = \frac{1}{\sqrt{KLC_{II}}} \quad (2.15)$$

The damping of the resonant circuit is represented by D , and it is expressed as [10]:

$$D = \frac{\sqrt{K}}{2} \left(\frac{\sqrt{\frac{L}{C_{II}}}}{R_{II}} + \frac{R}{\sqrt{\frac{L}{C_{II}}}} \right) \quad (2.16)$$

For a low noise coil $R \ll R_{II}$, so K can be assumed to be 1. Therefore the approximated damping coefficient becomes:

$$D = \frac{\sqrt{\frac{L}{C_{II}}}}{2R_{II}} \quad (2.17)$$

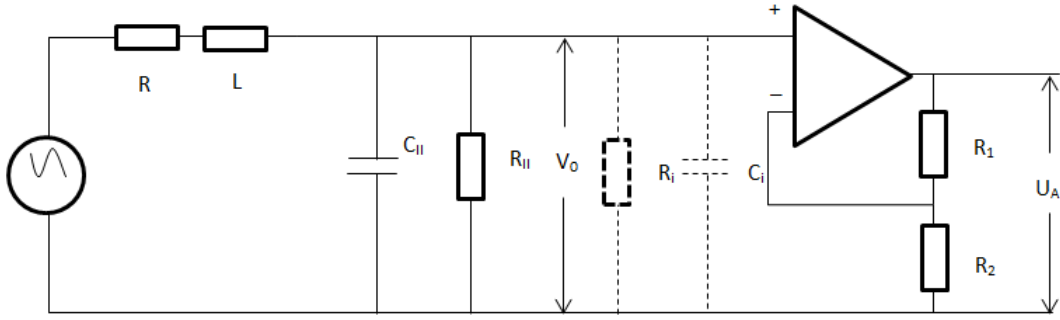


Figure 2.6: Induction Coil Connected to a Voltage Amplifier

If the sensor is tuned to resonance frequency w_r , then the magnitude of $F(w)$ becomes:

$$|F(w_r)| = \frac{R_{II}}{\sqrt{\frac{L}{C_{II}}}} = R_{II} \sqrt{\frac{C_{II}}{L}} \quad (2.18)$$

Then using (2.15):

$$R_{II} \sqrt{\frac{C_{II}}{L}} = \frac{R}{w_r L} \quad (2.19)$$

which indicates that the quality factor of the induction coil that is connected to a parallel resonant circuit is inversely proportional to its frequency dependent transfer function $F(w)$ at the resonance frequency [26]. However, $F(w)$ reaches its maximum value at resonance since the denominator term is minimized.

2.3.2 Series Resonant Circuit

The series resonant circuit is to be connected to a low input impedance (current) amplifier. The schematic of the circuit including a basic current amplifier stage is shown in Figure 2.7. R_1 is the feedback resistance in this configuration and series capacitance of the coil can be neglected. Output voltage of the circuit with respect to angular frequency can be assumed as in equation (2.8), however the transfer function

$F(w)$ in V_0 changes:

$$iF(w) = -\frac{R_1}{A(R_s + iwL)} \quad (2.20)$$

where R_s term is the total resistance in series with the coil inductance L and the denominator term in (2.18) indicates that the quality factor is in the form of voltage division. R_s can be expressed as:

$$R_s = R + \left(\frac{R_1}{A}\right) \quad (2.21)$$

In this configuration there is no shunt capacitance, the high pass filtering will not be observed. In order to obtain the ideal results, the amplifier should have a large bandwidth. In order to satisfy this condition, R_1/R ratio cannot be very high. However R and R_1/A can be neglected compared to wL term especially at higher frequencies at resonance frequency. Therefore at the resonance frequency, transfer function becomes:

$$iF(w) = -\frac{R_1}{A(iwL)} = i\frac{R_1}{A(wL)} \quad (2.22)$$

Then in final form F is:

$$F(w) = \frac{R_1}{A(wL)} \quad (2.23)$$

The Q of the series resonant circuit is:

$$Q = \frac{w_0L}{R} \quad (2.24)$$

which indicates that the quality factor of the induction coil that is connected to a series resonant circuit is actually inversely proportional to its frequency dependent transfer function $F(w)$ at the resonance frequency.

2.3.3 Frequency Response Comparison of Parallel and Series Resonant Circuit

For both series and parallel configurations, the output voltage is inversely proportional to the quality factor of the circuit. To maximize the absolute value of $F(w)$, the circuit is required to be tuned to the resonance frequency.

The parallel resonant circuit includes components R_{II} and C_{II} which introduces a low-pass filter to the circuit, also leading to frequency response having a peak value at the resonance frequency. Therefore tuning the circuit to the resonance frequency is

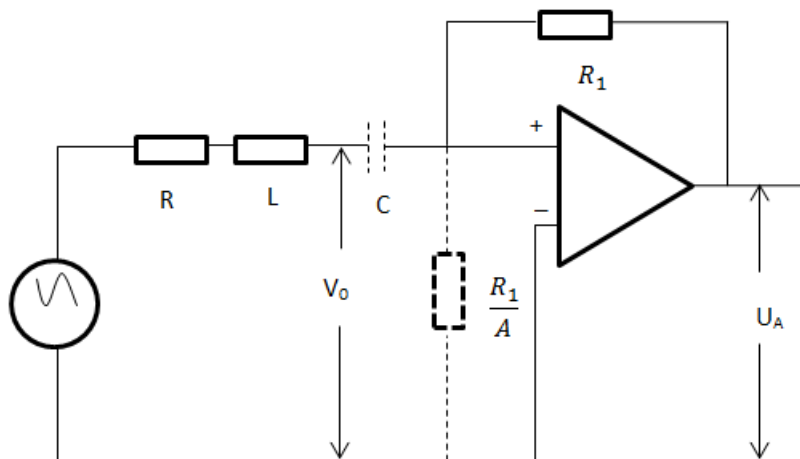


Figure 2.7: Induction Coil Connected to a Current Amplifier

extremely critical for the best performance in terms of sensitivity for this configuration.

The series resonant circuit has no shunt capacitance or resistance, causing the frequency response to have no upper band limitation. This provides a very wide bandwidth, however it has a drawback in terms of sensitivity. The comparison between the frequency responses of series resonant circuit and parallel resonant circuit is given in Figure 2.7. The same coil is used in both configuration types and the results are obtained with a software developed on MATLAB platform. Another difference between the two configurations is the tuning method. In parallel configuration, tuning capacitance is connected in parallel to the capacitance in the equivalent circuit. Therefore the total capacitance in the system is increased in an attempt to increase the value of the transfer function according to (2.18). This is more beneficial when the coil self resonance frequency is greater than the operating frequency since the increase in sensitivity comes both from the system approaching resonance(2.15) and the increase in the transfer function.

In series configuration, the shunt capacitance of the coil is neglected and the tuning capacitance is connected in series to the equivalent circuit of the coil. In this configuration, the total capacitance is decreased in an attempt to increase the resonance

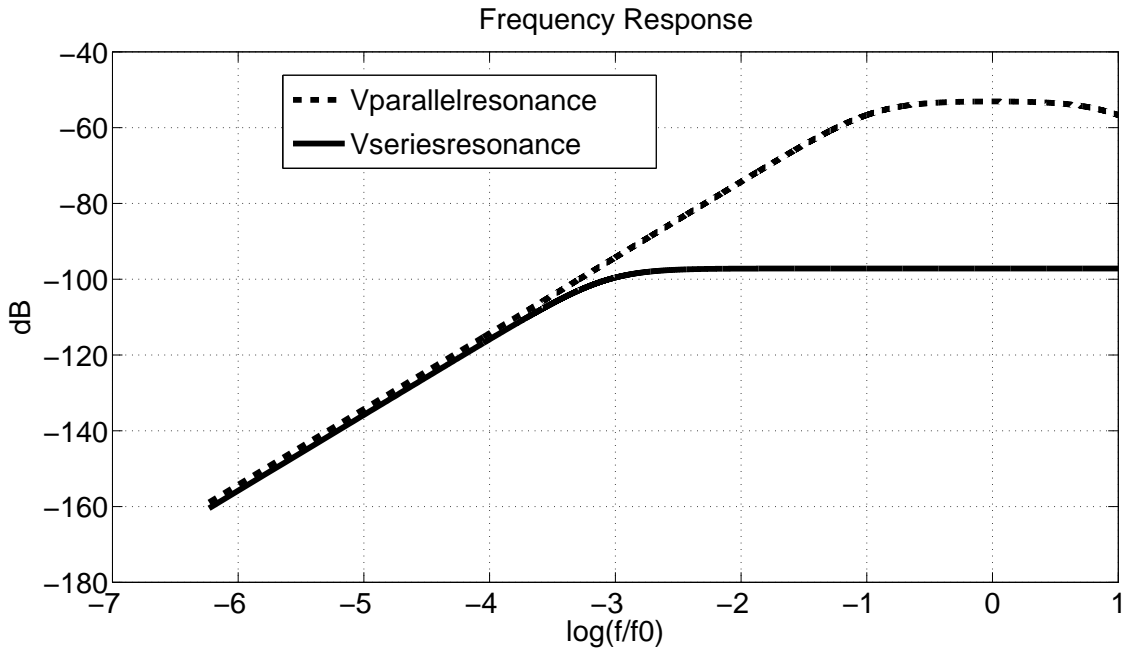


Figure 2.8: Comparison between the Frequency Responses of Parallel Resonance and Series Resonance Configurations. Results are obtained for 1 nT input and an amplification factor of 20. The parallel resistance R_{II} is 100Ω .

frequency, tuning the circuit at a higher frequency level. This also provides a low-pass filtering effect which can increase the sensitivity at the newly obtained resonance frequency while losing bandwidth.

Although series resonant connection can benefit from improvements due to its frequency response and the biomedical applications requiring high operating frequency, in terms of sensitivity, the performance decrease significantly as suggested in Figure 2.8. Another reason for choosing the parallel configuration is that the applications of interest do not require high bandwidth. Therefore if the circuit can be tuned at a sufficiently high frequency, parallel resonant circuit provides a greater sensitivity, which is critical for almost every biomedical magnetic sensor application.

2.4 Frequency Related Parameters

As indicated in (2.15), there are three main parameters that affect the frequency response of the circuit. These are the voltage division factor K , coil inductance L and the total capacitance C of the amplifier circuit.

2.4.1 K Parameter

The K parameter as given in (2.14), depends on the resistance of the coil and the damping resistor whose purpose is to adjust the frequency dependent transfer function $F(w)$. However the addition of the damping resistor is based on the assumption that the input resistance of the amplifier stage is high, therefore when connected in parallel, effect of R_i would be negligible. If R_i is not sufficiently high, then the total shunt resistance R_{II} is actually a combination of R_i and the damping resistance.

In biomedical applications of induction coil, requirements due to the sensitivity and SNR properties encourage the use of low-noise coils. The noise caused by the induction coil is mainly the thermal noise that is directly proportional to the DC resistance of the circuit. Since obtaining the minimum noise is critical, coil resistance should be kept as small as possible leading the K value to be approximately 1.

The resistance of an induction coil has two components namely: DC resistance and AC resistance. The DC resistance depends on the resistance of the wire wound in the coil. It can be expressed as:

$$R_{dc} = \frac{l_w}{\sigma A} \quad (2.25)$$

where l_w is the total wire length, σ is the conductivity of the wire, and A is the wire area. For multilayer coil l_w would be:

$$l_w = \pi \frac{D + D_i}{2} n \quad (2.26)$$

The cross sectional area of the wound wire in terms of its diameter is:

$$A = \pi \left(\frac{d}{2} \right)^2 \quad (2.27)$$

Then combining (2.26) and (2.27) into (2.25) and recalling (2.5), DC resistance is then in terms of coil parameters [8]:

$$R_{dc} = \frac{(D + D_i)(D - D_i)l}{\sigma k d^4} \quad (2.28)$$

For flat spiral coil, l_w would be:

$$l_w = \pi n(D + (d + s)(n - 1)) \quad (2.29)$$

leading to DC resistance to become:

$$R_{dc} = \frac{\pi n(D + (d + s)(n - 1))}{\sigma \pi d^2} \quad (2.30)$$

The thermal noise caused by the DC resistance of the coil in terms temperature and frequency is:

$$U_n = \sqrt{(u_n)^2} = \sqrt{4k_B T R_{dc} \Delta f} \quad (2.31)$$

where k_B is the Boltzmann constant, T is temperature in Kelvin and Δf is the frequency bandwidth. Therefore from (2.31), it can be observed that temperature, bandwidth and the DC resistance are the factors that can increase the thermal noise of the induction coil. This also proves that the DC resistance of the coil should be minimized for the induction coil sensor to be able to sense signals of small magnitude. The noise level of the induction coil and its comparison to the signal level will be discussed thoroughly in the next chapter.

The AC resistance of the induction coil is caused by the variation of the magnetic field through the inductor leading to change in current density in different regions of the wire. This difference in current density between inner and outer regions of the wire is called skin effect. However when multilayer coils are the case, there is another dominating modification on the resistance which is called proximity effect. It is caused by the constrain of current distribution within the first conductor to smaller regions. There is a model that includes both effects and modify the DC resistance accordingly. It is called Dowell Method [27], where the round wires are approximated by an equivalent foil of rectangular wires, and a one dimensional solution is done afterwards.

The total resistance of a multilayer coil is in terms of DC resistance:

$$R_{AC} = R_{DC} \left(\phi \left[G_1(\phi) + \frac{2}{3}(n_l^2 - 1)(G_1(\phi) - 2G_2(\phi)) \right] \right) \quad (2.32)$$

where n_l is the number of layers and ϕ is the correction factor due to the rectangular wire replacement which is:

$$\phi = \left(\frac{\sqrt{\pi}}{2} \right) \left(\frac{d}{\delta} \right) \quad (2.33)$$

In this equation, δ represents skin depth, which proves that the skin effect is covered in (2.32). Skin depth can be expressed as:

$$\delta = \frac{1}{\sqrt{\pi f \mu \sigma}} \quad (2.34)$$

G_1 and G_2 are equations expressing the geometry of infinite conducting foil:

$$G_1(\phi) = \frac{\sinh(2\phi) + \sin(2\phi)}{\cosh(2\phi) - \cos(2\phi)} \quad (2.35)$$

$$G_2(\phi) = \frac{\sinh(\phi)\cos(\phi) + \cosh(\phi)\sin(\phi)}{\cosh(2\phi) - \cos(2\phi)} \quad (2.36)$$

Therefore computing (2.33), (2.34), (2.35), (2.36) and (2.30), then using the results in (2.32) gives the approximate resistance of a multilayer coil. However discrepancy is expected since the approximation is one dimensional to a three dimensional problem. The model is accurate enough to use in design equations and the include of proximity effect is extremely important in high frequency sensor applications that is affected by quality factor such as wireless power transfer, since it depends heavily on resistance. The accuracy of the Dowell method will be further discussed in experimental work part by comparing the measured and calculated coil resistance values.

2.4.2 Inductance Parameter

The inductance of an air-cored coil is highly dependent on turn number, coil diameter and slightly dependent on inner coil diameter and wire diameter. Inductance increases with the square of the turn number and diameter.

Inductance of a single turn circular loop if $D \gg d$ [9]:

$$L = 6.28D \left(\ln \frac{8D}{d} - 2 + a \right) 10^{-9}[H] \quad (2.37)$$

where a is the factor representing the skin effect. Since the induction coils with multilayer winding design is of interest, the inductance of such a coil can be calculated under the assumption $D \gg l$ using:

$$L = \frac{78.7 \left(\frac{D+D_i}{2} \right)^2 n^2}{3 \frac{D+D_i}{2} + 9l + 10(D - D_i)} nH \quad (2.38)$$

This formula is very critical for designing a multilayer disk shaped induction coil and a small experiment to prove the accuracy of this formula will also be given at the experimental work section.

For the case of flat spiral coil, the inductance is calculated using [28]:

$$L = \frac{an^2}{8a + 11b} \mu H \quad (2.39)$$

where $a = (D + D_i)/4$ and $b = (D - D_i)/2$, all dimensions are in inches.

Increase in inductance is extremely undesirable since it both reduces the resonance frequency, forcing the operating frequency to be also lowered and recalling (2.18), the inductance also decreases the transfer function $F(w)$ output of the coil. Therefore according to (2.38), even though mean diameter of the coil greatly increase the output signal of the sensor, the need to minimize the turn number can be understood. This is one of the reasons thicker wires are preferred in the probable coil designs in some biomedical applications.

2.4.3 Capacitance Parameter

The final parameter to be examined in (2.15) is the capacitance of the coil. In a multilayer solenoid, there are two kinds of capacitance: Distributed capacitance between two adjacent turns and two adjacent layers. The lumped self capacitance of the coil depends on the operating frequency and reaches its maximum at the resonance frequency. However this variation with the frequency is relatively small and can be neglected, leading to a constant frequency capacitor model. However it is very

difficult to obtain a formula that gives the self capacitance C due to the fact that it is affected by many internal parameters like style of winding, presence of insulation etc. This is actually the most challenging aspect of the coil design.

Due to the need of high resonance frequency in the applications of interest, capacitor should be minimized. This also improves sensitivity in a way by avoiding the restriction of minimizing the inductance, further allowing the increase in turn number and coil mean diameter which will provide valuable increase in the output voltage of induction coil as indicated in (2.9). Therefore it is important to be able to design the coil capacitance as accurate as possible.

There are various formulas for self-capacitance of an air-cored multilayer solenoid which are relatively accurate for certain conditions. Due to these formulas being unreliable, the experimental way to obtain the capacitances is used to verify the accuracy of the formulas. This method is explained in the experimental work section in detail.

Three equations to obtain the self-capacitance of the induction coil are to be examined and compared in this study. First one is [10]:

$$C = \frac{\pi \varepsilon_0 \varepsilon_r l}{t(n_l - 1)} \left(\frac{D + D_i}{2} + 2n_l(d + t) \right) \quad (2.40)$$

where ε_0 is the electric permittivity of free space and ε_r is the relative electric permittivity and t is the thickness of the wire insulation. All dimensions in (2.40) are to be measured in meters. Moving on to the second equation [1]:

$$C = \frac{0.37 \frac{D+D_i}{2} \varepsilon_r l}{2tn_l} [pF] \quad (2.41)$$

All dimensions in (2.41) are to be measured in cm. Third and final equation [12]:

$$C = \frac{0.3Pl\varepsilon_r}{tn_l} [pF] \quad (2.42)$$

P is the mean circumference of the coil and all the dimensions to be measured in (2.42) are in inches.

All three formulas indicate that the capacitance is directly proportional to the axial length and the mean diameter of the coil. On the other hand, it is inversely proportional to the number of layers and the insulator thickness. Relative electric permittivity of the insulator also increases the capacitance. The effect of the parameters for all three equations are the same, however different constants are used in these equations which make them more accurate at certain frequency ranges. These will be analyzed along with the experimental capacitance measurement technique in the experimental work chapter.

For flat spiral coil case, turn to turn capacitance is calculated according to the equation [29]:

$$C = \varepsilon_0 l_w \frac{2\varepsilon_r \arctan\left(\frac{(-1+\sqrt{3})(2\varepsilon_r + \ln \frac{d_o}{d})}{(1+\sqrt{3})\sqrt{\ln \frac{d_o}{d}(2\varepsilon_r + \ln \frac{d_o}{d})}}\right)}{\sqrt{\ln \frac{d_o}{d}(2\varepsilon_r + \ln \frac{d_o}{d})}} [pF] \quad (2.43)$$

Total capacitance can be obtained by multiplying the turn to turn capacitance with $n - 1$.

2.5 Magnetic Field Produced by an Induction Coil

To be able to calculate the magnetic field produced by an induction coil is useful and necessary for some applications. This calculation will also be necessary for the basic test setup that will be given in the experimental work part.

From Ampere's Law, the magnetic field at the center of a current loop is:

$$B = \frac{\mu_0 I n}{l} \quad (2.44)$$

where I is the current per turn. The magnetic field on the axis of a current loop which is illustrated in figure 2.9 can be obtained using Biot-Savart Law:

$$dB_x = \frac{\mu_0 I a dL}{4\pi(\rho^2 + a^2)^{3/2}} \quad (2.45)$$

dB_y components around the x-axis cancel out each other due to the symmetry along x axis therefore the only component of the on-axis field is the dB_x component. Afterwards, integrating along the x axis results in:

$$B_x = \int dB_x = \frac{\mu_0 2\pi I a^2}{4\pi(\rho^2 + a^2)^{3/2}} = \frac{\mu_0 I a^2}{2(\rho^2 + a^2)^{3/2}} \quad (2.46)$$

However in the case of a multilayer solenoid, dI changes due to the included parameters such as D and D_i . The magnetic field produced on the axis of an air-cored multilayer solenoid can be obtained from the sum of the fields on the individual turns. The current inside the area $dxdy$ on the coil can be expressed as [11-12]:

$$dI = \frac{nI dxdy}{b - a} \quad (2.47)$$

Therefore dB now becomes:

$$dB = \frac{\mu_0 n I y^2 dxdy}{2(b - a)(x^2 + y^2)^{3/2} l} \quad (2.48)$$

Integrating over the cross section of the coil, total field can be obtained as:

$$B = \frac{\mu_0 n I}{2(b - a)l} \int_b^a y^2 dy \int_{x_1}^{x_2} \frac{dx}{(x^2 + y^2)^{3/2}} \quad (2.49)$$

In order to integrate, first $x = y \tan \theta$ substitution is used leading to second integral to be:

$$\left[\frac{x}{y^2 \sqrt{x^2 + y^2}} \right]_{x_1}^{x_2} \quad (2.50)$$

then the first integral can be obtained using:

$$\int \frac{dy}{\sqrt{x^2 + y^2}} = \ln(y + \sqrt{x^2 + y^2}) \quad (2.51)$$

Therefore the resultant equation for B at any point on the axis of the solenoid is:

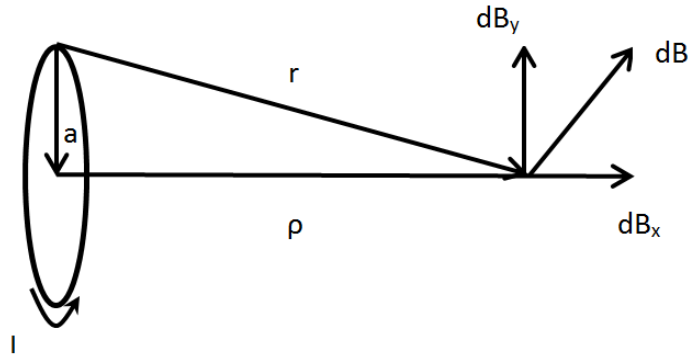


Figure 2.9: Magnetic Field on the Axis of a Current Loop

$$B = \frac{\mu_0 n I}{2(b-a)l} \left[x_2 \ln \left(\frac{b + \sqrt{b^2 + x_2^2}}{a + \sqrt{a^2 + x_2^2}} \right) - x_1 \ln \left(\frac{b + \sqrt{b^2 + x_1^2}}{a + \sqrt{a^2 + x_1^2}} \right) \right] \quad (2.52)$$

The parameters are illustrated in figure 2.10

In the figure 2.10, specified parameters x_1 and x_2 are indicating the position of the both ends of the solenoid. b is the outer radius and a is the inner radius. r is the distance between a point inside the solenoid and a point on the axis of the solenoid.

The use of (2.52) in a simulation software developed using MATLAB with varying position on the axis, after being applied to an air-cored solenoid with 0.25 cm length, 2 cm outer and 0.4 cm inner diameter, the resultant magnetic field behavior versus the position is illustrated in figure 2.11. x_1 is the x_2 is the addition of the values of position x starting from the center of the coil and the coil length l .

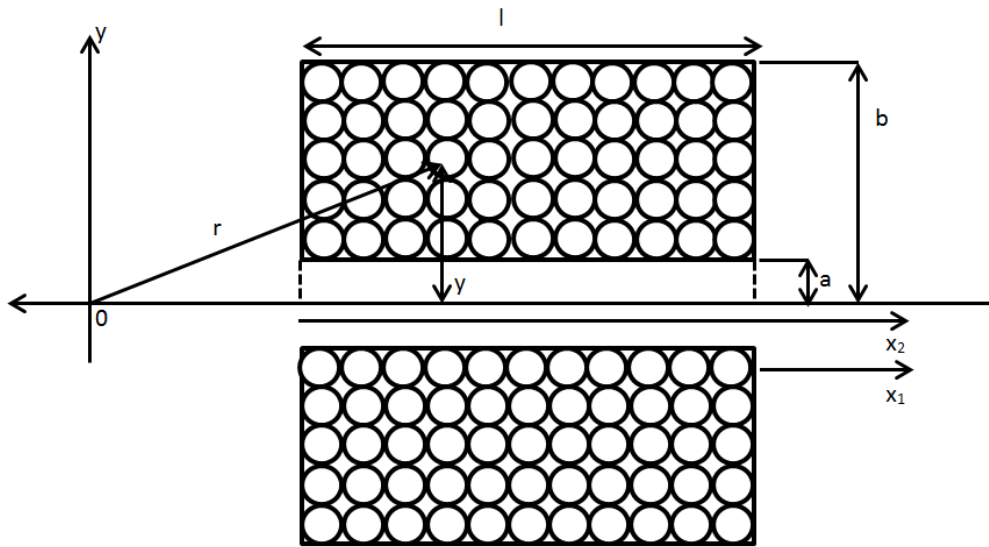


Figure 2.10: Magnetic Field on the Axis of a Multilayer Air-Core Solenoid

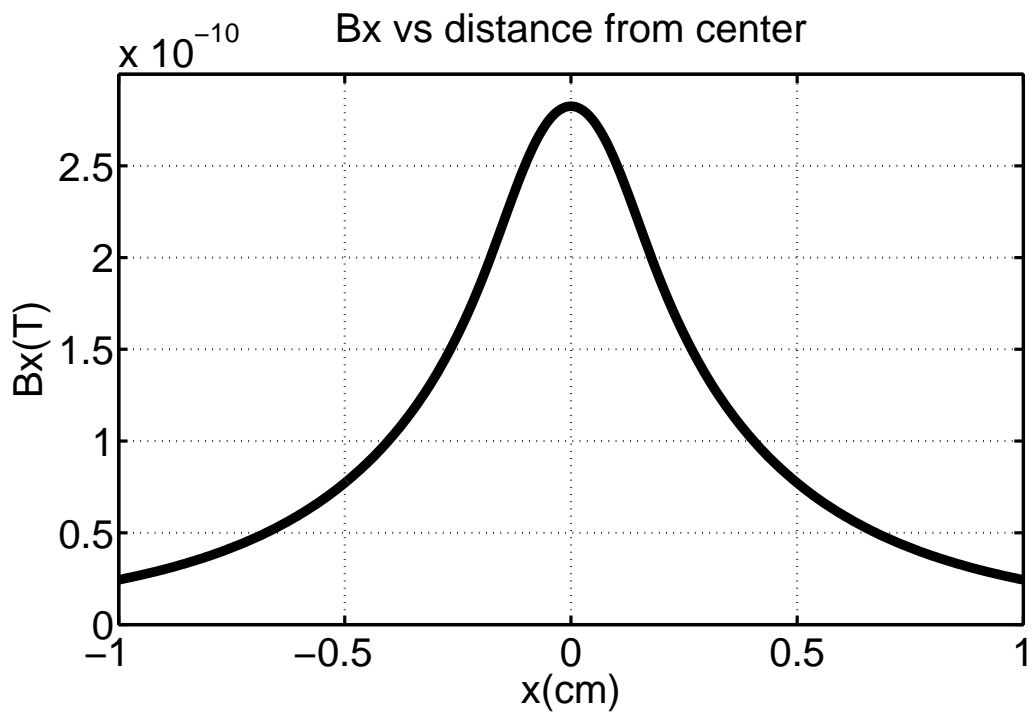


Figure 2.11: Magnetic Field on the Axis of an Induction Coil vs position

CHAPTER 3

DESIGN OF THE MAGNETIC SENSOR

3.1 Introduction

The next step is the design of magnetic sensor using a multi-turn circular coil (Figure 2.1). To be able to provide an accurate design procedure, MATLAB is used, first to investigate the effects of certain coil parameters, then to develop an optimization software using all equations given so far.

Therefore, firstly the coil parameters and their effects will be discussed. Then the optimization software will be explained. After a brief explanation is given about the experimental work that is intended to be done in this study, the amplifier design and requirements will be examined. Finally, the frequency response of the sensor circuit connected to the amplifier will be illustrated.

3.2 The Effect of Coil Parameters

There are mainly three multilayer induction coil parameters: mean diameter, coil length and wire diameter. Their effects on measurement performance is observed in this section. In order to provide an accurate design, the circuit is actually tuned at the resonance. So for every parameter, it is expected that an optimum point is to be reached.

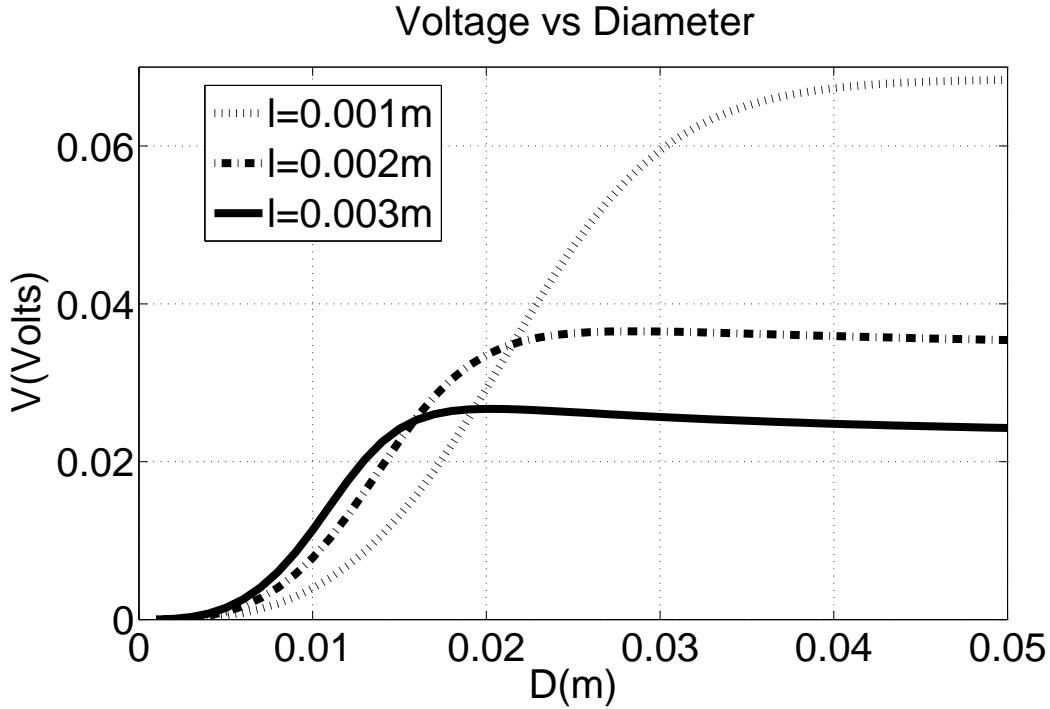


Figure 3.1: Output voltage versus coil diameter for different coil lengths

3.2.1 Coil Diameter

As indicated in equation (2.7), the output voltage of an induction coil is directly proportional to the mean diameter. However, too much increase can result in a decrease in the resonance frequency, forcing the designer to work at a lower operating frequency. The tests in this section are made at 1 MHz operating frequency condition. This balanced structure is illustrated in Figure 3.1. It can be observed that the output voltage is better for different coil lengths at certain D values, for example at $D=0.02$ m, $l=0.002$ m should be chosen among the three, however at $D=0.04$ m, $l=0.001$ m should be chosen for a better performance. For instance at $D=0.016$ m, 0.002 m long coil performs the best, however for lower coil diameters a longer coil performs better and at higher coil diameters, a shorter coil performs much better. This implies an optimum range of turn number. Wire diameter d is constant and 0.6 mm through the process. This information is useful while developing the optimization software.

3.2.2 Coil Length

In equation (2.7), it is observed that the coil length has relatively smaller effect. It has a contribution though, through the increase in turn number. It also increases inductance and capacitance which decreases the resonance frequency, and is undesirable. Figure 3.2 shows coil voltage V versus coil length l plots for different coil diameters D . Results are similar to the previous case in terms of coils of different diameters performing the best at different coil length ranges. This again implies the existence of an optimum turn number.

3.2.3 Wire Diameter

Wire diameter d , as mentioned in equation (2.7), has a great effect on turn number n , however, it does not affect other parameters individually. Due to its effect on the turn number, there is a clear optimum point for every coil diameter and length combination. Two different examples are given in Figure 3.3a and b. These and other results suggest that wire diameter is the parameter to start the optimization. It is computationally easier to get a maximum point for every parameter combination when the wire diameter varies since it only affects the turn number. Therefore the variation of wire diameter is used as the inner member of the loop hierarchy. The next section will include a MATLAB software developed to obtain the parameters for the best sensitivity.

3.3 Coil Parameter Optimization

According to the data obtained through previous sections, it can be deduced that the design of a coil with optimum sensitivity for a specified operating frequency can be achieved. The behavior of the output voltage due to the change in wire diameter shapes the code yielding the d loop as the inner loop. Outer loops are the coil diameter D and coil length l . The maximum output voltage value is obtained among d variation for each D and stored according to the indices of D . Then the same procedure is applied for l until the greatest output voltage is obtained. Then using all of the

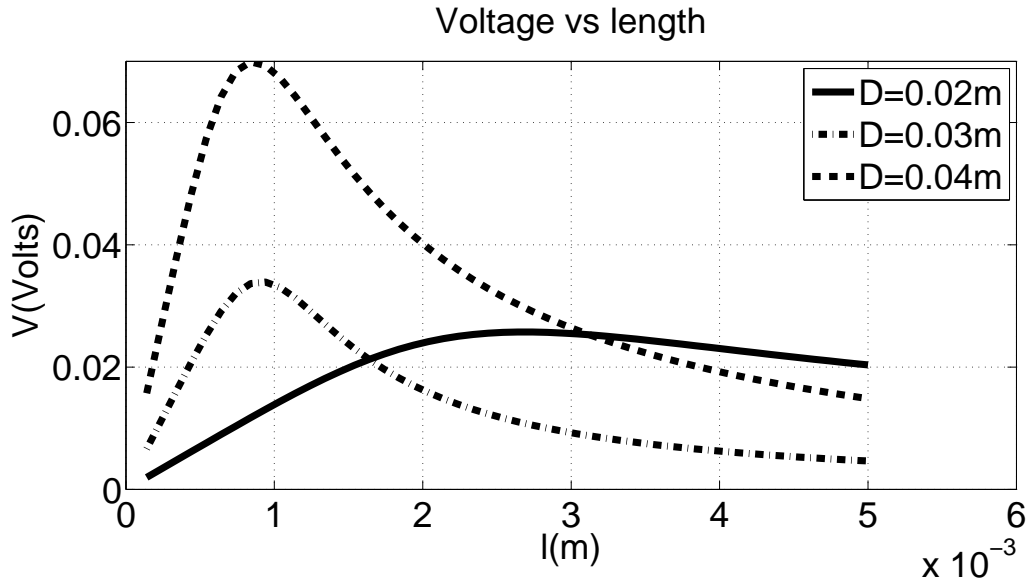
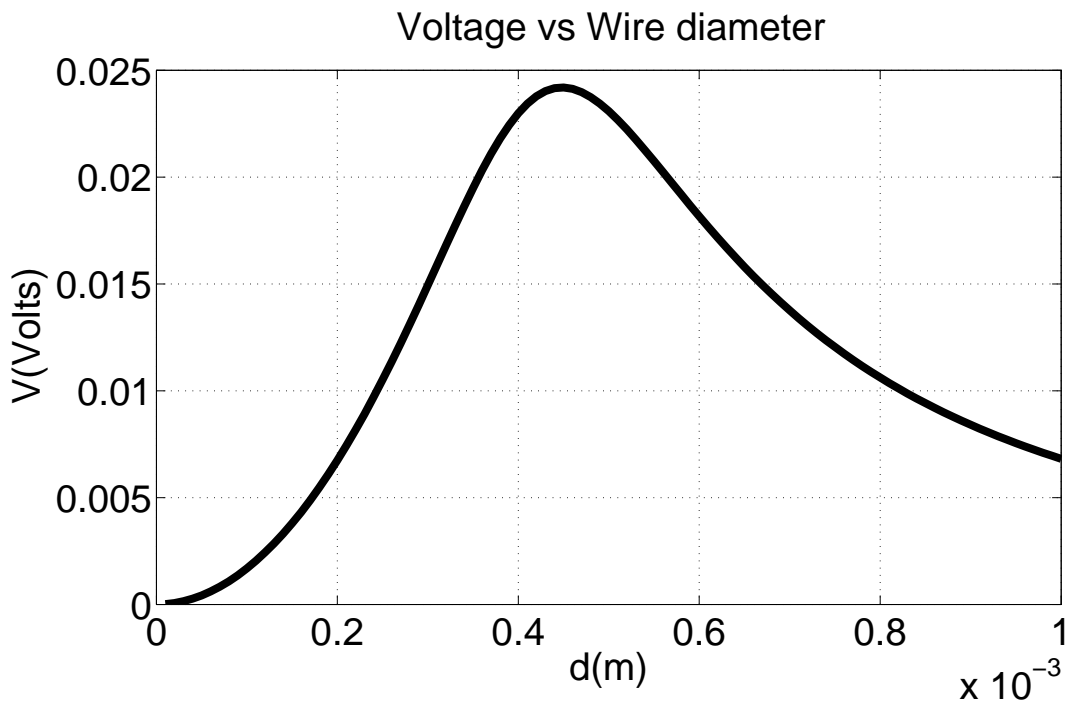


Figure 3.2: The effect of coil length

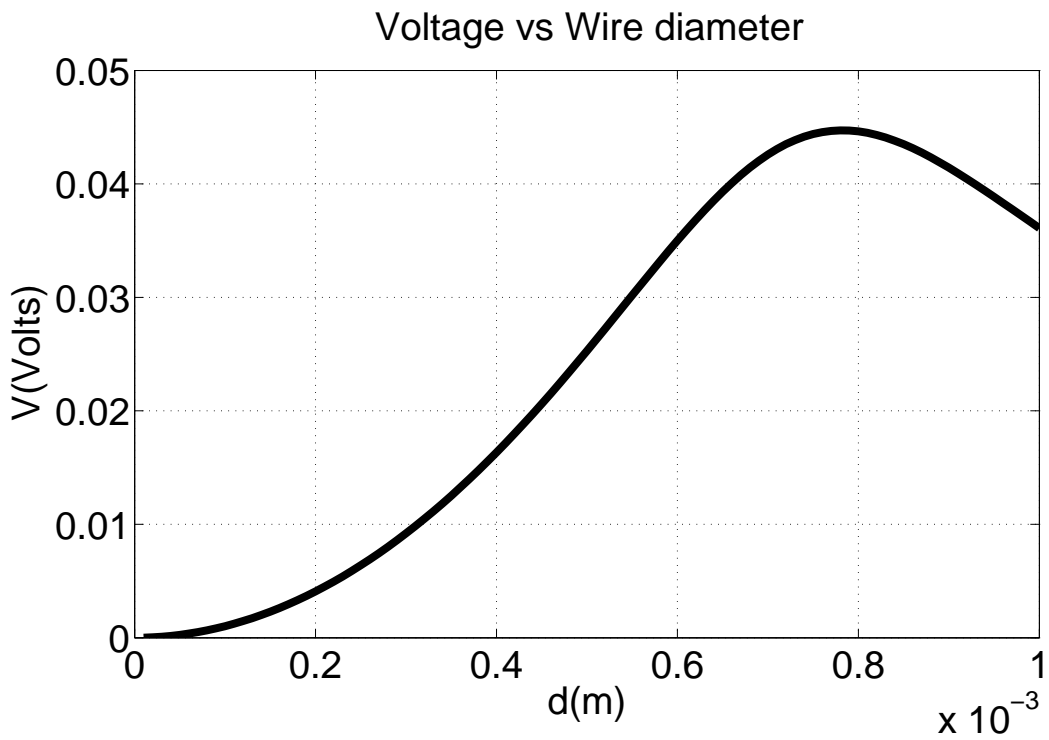
stored indices, the coil parameters for the maximum voltage is obtained, rendering the optimization complete for a given frequency.

Therefore, it is possible to design an optimized coil for various operation frequencies and applications. This software is used to design measurement coils for LFEIT and after the optimum coil is specified, its performance will be discussed.

Figure 3.4 shows the graphical user interface (GUI) of the MATLAB software for a specific set of coil parameters. This software determines the optimum coil size parameters for an operating frequency and size constraints. Graphs on the figure further verifies the size parameters that provide optimum sensitivity. The input magnetic field is 100 pT and amplifier gain A is set to a value of 2000 V/V. Operating frequency of this test case is chosen as 0.5 MHz. Maximum coil diameter is given as 0.01 m and maximum wire diameter is specified as 0.002 m. The graphs indicate that there is an optimum point in terms of coil diameter at 0.01 m. This means that in order for the optimization to occur, a maximum coil diameter constraint is necessary. This is also meaningful since the output voltage of the coil sensor increases with coil diameter. The diameter of the coil will be limited due to the nature of the application where the sensor is used. After the maximum coil diameter constraint is applied, an appro-



(a) $l = 0.0012\text{m}, D = 0.02\text{m}$



(b) $l = 0.002, D = 0.03\text{m}$

Figure 3.3: Wire diameter vs output voltage for different coil diameter and length combinations

priate coil length and wire diameter for the optimum output voltage is determined by the software. These parameter values for maximum output voltage are the results of interest. The magnitude of the maximized voltage is also computed. Therefore as shown by the test case results, a maximum output voltage of 0.0024 Volts can be obtained using an air-cored multilayer coil.

Specifications of different wireless power transfer applications require coil sensor designs for a wide range of operating frequencies. Therefore, further improvement on the GUI software is done to determine the optimum coil type and its parameters. Improved GUI determines whether air-cored multilayer coil or flat spiral coil performs better and specifies an optimum coil, also providing its parameters. These features are added and new GUI with two different example cases are given in Figure 3.5 and Figure 3.6. These examples show that at 10 MHz operating frequency, using flat spiral coil is more advantageous, whereas at 100 kHz operating frequency, multilayer coil holds better results. Note that, flat spiral coil does not have a coil length parameter and multilayer coil does not have turn spacing parameter. This improved GUI will prove very useful due to the fact that certain wireless power transfer applications work at higher operating frequencies, flat spiral coil is proven to perform much better than its multilayer counterpart.

3.4 Amplifier Design

Due to their low pass filter behavior, OP-AMPs will have their gain reduced after a certain frequency. Since the operating frequency required by the biomedical applications are usually high, the amplifier should be chosen carefully in order to obtain sufficient gain. AD797, which is actually a low-noise, high input impedance OP-AMP that suits very well for the desired purpose except for its insufficient bandwidth. This causes AD797 to perform better than many of its counterparts, however its gain is still not enough for applications which require high sensitivity..

The high frequency behavior of a voltage amplifier OP-AMP can be explained with the following equation [13]:

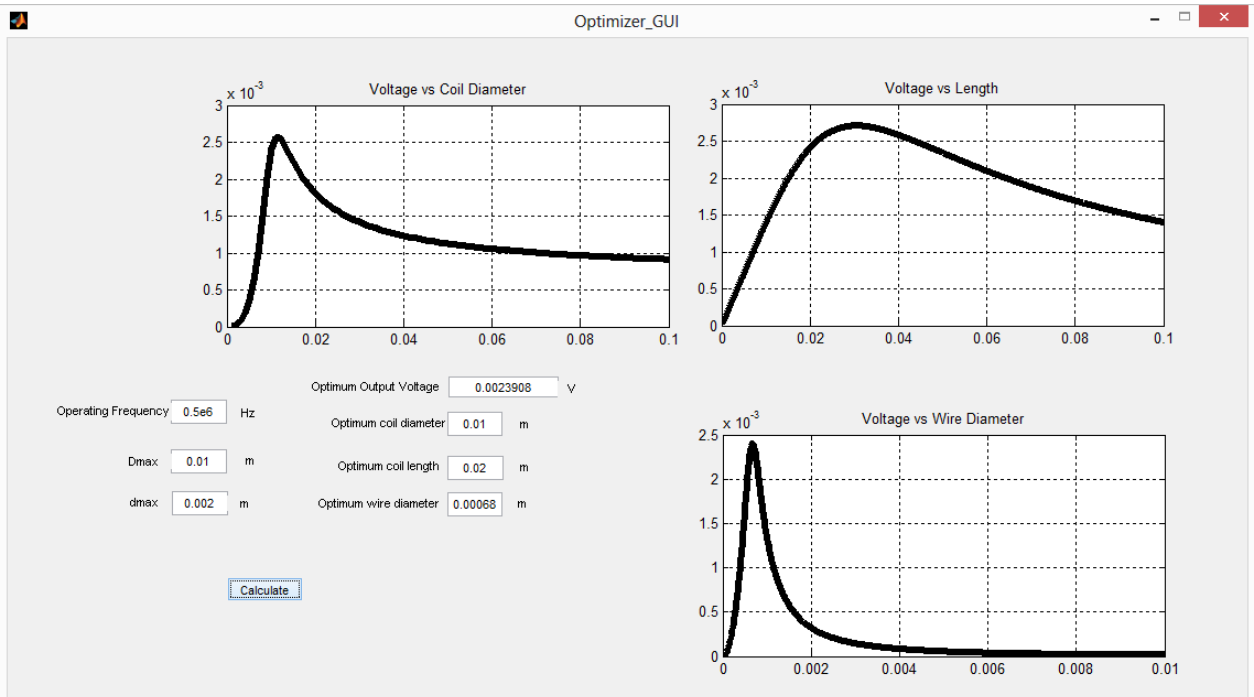


Figure 3.4: Optimization GUI Software

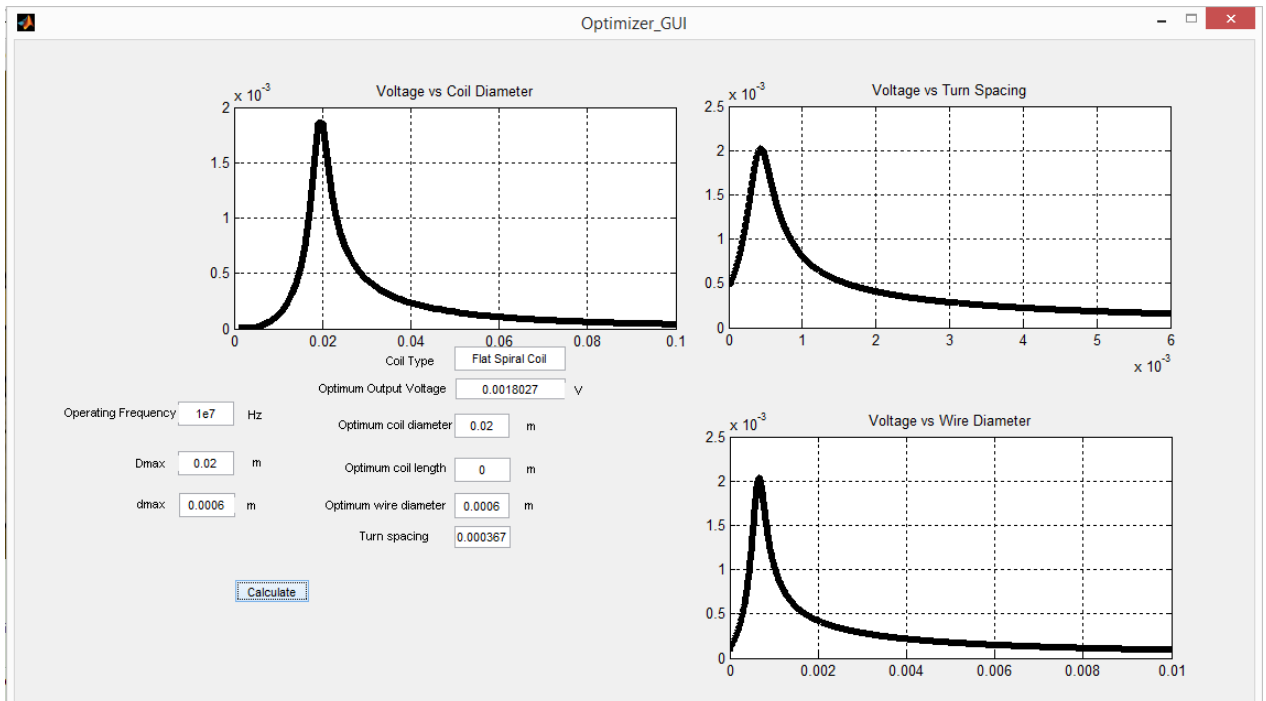


Figure 3.5: Improved optimization GUI software example 1

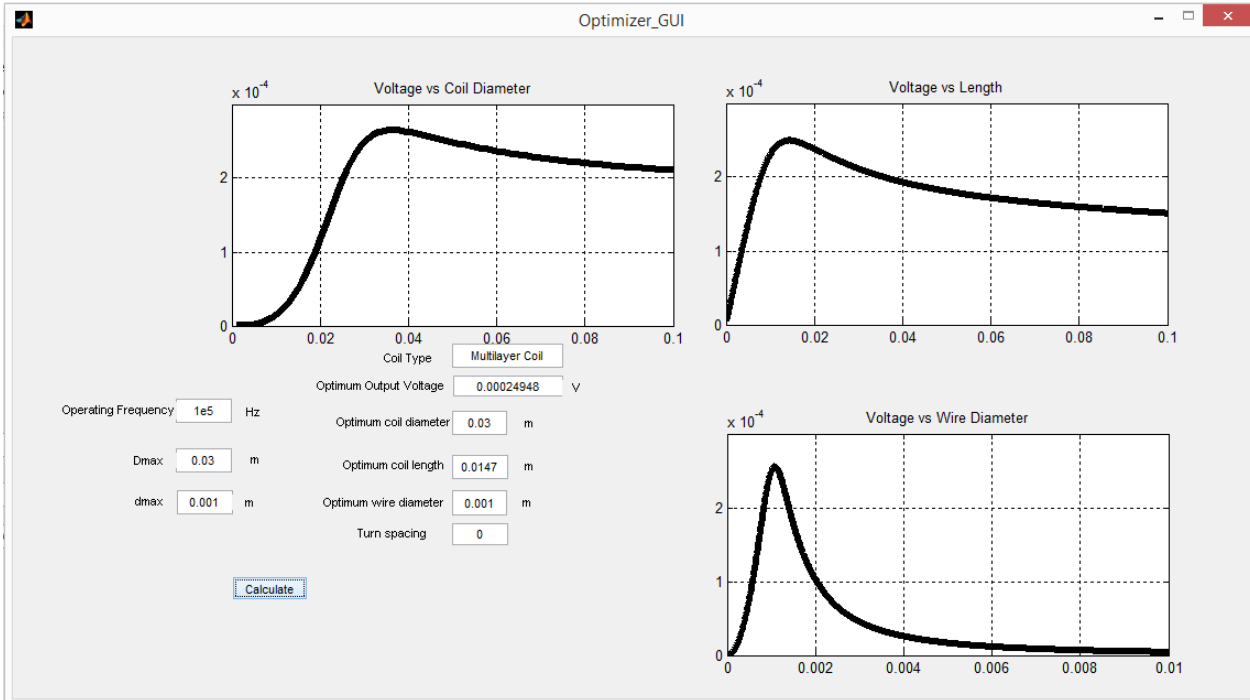


Figure 3.6: Improved optimization GUI software example 2

$$A_v = \frac{G_0}{1 + G_0\gamma} \quad (3.1)$$

where A_v is the closed loop gain of the OP-AMP, G_0 is the open loop gain and the γ is the feedback factor. Closed loop gain A_v also has a relationship with the frequency such as:

$$GBP = A_v BW \quad (3.2)$$

where GBP is the gain-bandwidth product and BW is the bandwidth. The gain-bandwidth product is constant, and for AD797, it is specified in the datasheet as 110 MHz. G_0 and A_v decreases as the frequency increases for the whole frequency range for this OP-AMP. Therefore, for the case when the operating frequency is 2.2 MHz, G_0 is obtained as 52.2 using AD797 datasheet. According to this information, for $\gamma = 10^{-3}$, A_v is calculated as 50 using equation (3.2).

The circuit from Figure 2.6 is drawn in the simulation program multisim for its transient analysis. The results are shown in Figure 3.7. The smaller signal (V_6) is the

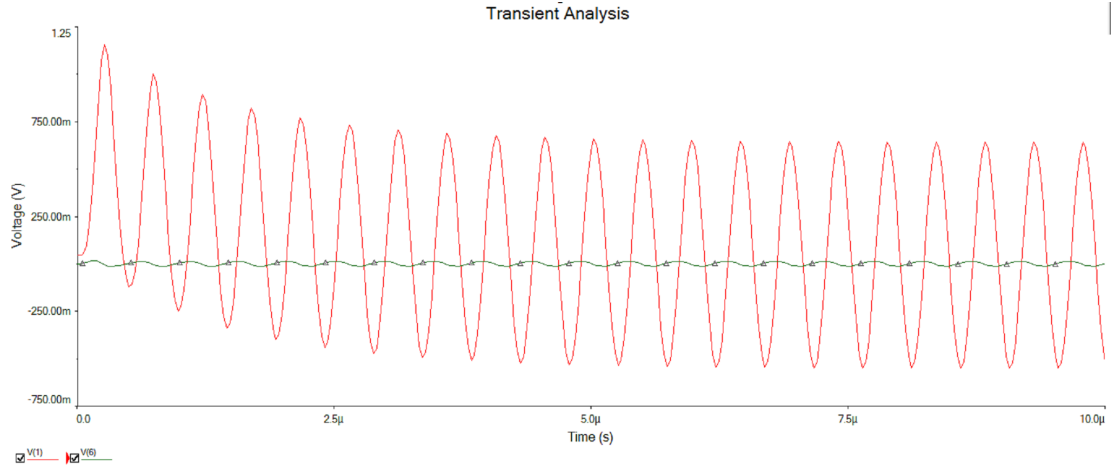


Figure 3.7: Transient analysis of amplifier circuitry. Simulation software used is multisim. Green signal is the input of the amplifier, indicated as V_6 . Red signal is the output of the amplifier, indicated as V_1 . The operating frequency used in the simulation is 2.2 MHz

input voltage and the greater one (V_1) is the output voltage. After the signal is stable, V_1 is obtained as $1.2 V_{pp}$ and V_6 is obtained as $24 mV_{pp}$ then their ratio becomes 50, which proves the relationship between the frequency and the open loop gain.

3.5 Frequency Response of the System and Noise Analysis

The sensor system has a bandpass characteristic. On the logarithmic frequency scale, the output reaches its maximum when $f = f_0$, as was illustrated in Figure 2.8.

The bandwidth of the system is important and the requirements change for different applications. If the bandwidth is high, the frequency range of operation for the system becomes wide. However it should be noted that high bandwidth causes the system noise to increase. Figure 3.8 shows the amplifier circuit with its equivalent noise sources referred to the input [10]. In this figure, $\sqrt{\frac{U_R^2}{\Delta f}}$ term is the thermal noise voltage caused by the coil resistance, $\sqrt{\frac{i_R^2}{\Delta f}}$ term is the thermal noise current due to the total shunt resistance, $\sqrt{\frac{U^2}{\Delta f}}$ and $\sqrt{\frac{I^2}{\Delta f}}$ are the series and shunt noise components caused by the amplifier.

The total noise power density can be expressed in terms of total noise voltage U_N [10]:

$$\frac{U_N^2}{\Delta f} = \frac{U^2}{\Delta f} + \frac{U_R^2}{\Delta f} [F(w)]^2 + \left[\frac{I^2}{\Delta f} + \frac{I_R^2}{\Delta f} \right] |Z|^2 [F(w)]^2 \quad (3.3)$$

where Z is the impedance of the coil. By neglecting the contribution of the capacitance at high operating frequencies, the coil impedance can be written simply as follows::

$$Z = R + j\omega L \quad (3.4)$$

The coil is designed to be low noise by keeping its resistance around a few ohms at maximum, which is another restriction upon the turn number recalling (2.20) and (2.21). As seen by the combined noise equation (3.3), there is also the need to use a low noise amplifier. It should also be noted that the noise is mainly of thermal characteristic and determined by the resistances included in the system. Thus it is nearly DC throughout the frequency band due to its AC component being too small to affect, except around the resonance frequency. This is because of the effect of $F(w)$ in (3.3).

The noise equivalent magnetic field can be obtained using the relationship between the sensitivity and the voltage:

$$S_0 = \frac{U_0}{fH} \quad (3.5)$$

where U is the voltage induced on the sensor coil due to the applied magnetic field H . If the sensor is assumed to be free of internal noise, the noise voltage at the output of the coil is:

$$\frac{U_0^2}{\Delta f} = \frac{1}{F(w)^2} \frac{U_N^2}{\Delta f} \quad (3.6)$$

Therefore combining (3.3), (3.5) and (3.6), the resultant equation for the noise equivalent magnetic field power spectral density is [10]:

$$\frac{H_N^2}{\Delta f} = \left(\frac{1}{S_0 f} \right)^2 \left[\frac{U^2}{\Delta f} [F(w)]^{-2} + \frac{U_R^2}{\Delta f} + \left(\frac{I^2}{\Delta f} + \frac{I_R^2}{\Delta f} \right) |Z|^2 \right] \quad (3.7)$$

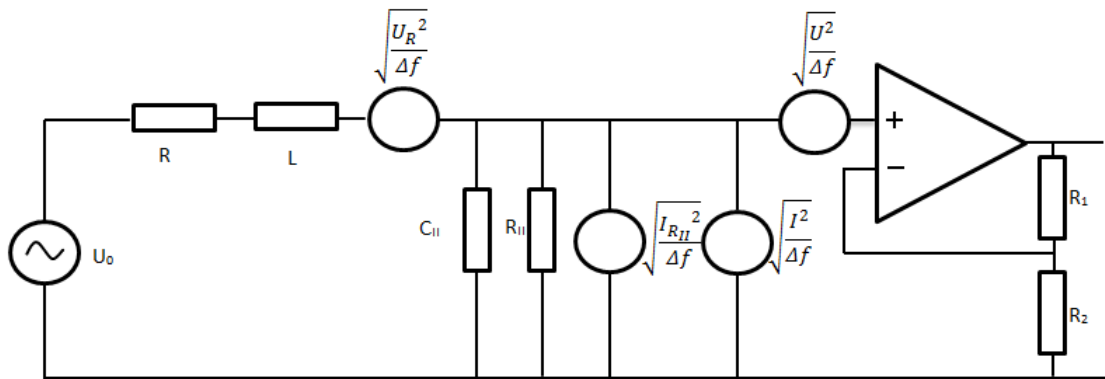


Figure 3.8: Noise equivalent circuit [10]. $\frac{U_R^2}{\Delta f}$ and $\frac{i_R^2}{\Delta f}$ are the noise voltage representing the thermal noise of the coil resistance R and the noise current representing the damping resistor R_{II} respectively. $\frac{U^2}{\Delta f}$ and $\frac{I_R^2}{\Delta f}$ represent the internal noise voltage and internal noise current of the amplifier

An illustration of the above explanations and equations is required. Thus a frequency sweep MATLAB code for the induction coil sensor is developed. The coil designed for LFEIT application is used in the simulation. The results are shown in Figure 3.9. It is observed that the noise does not depend on the frequency except around the resonance frequency for this application. This figure is obtained for 1 nT magnetic flux density as an input. The parallel resistance R_{II} is 100 Ω , causing the system to have relatively high bandwidth at the cost of lower sensitivity.

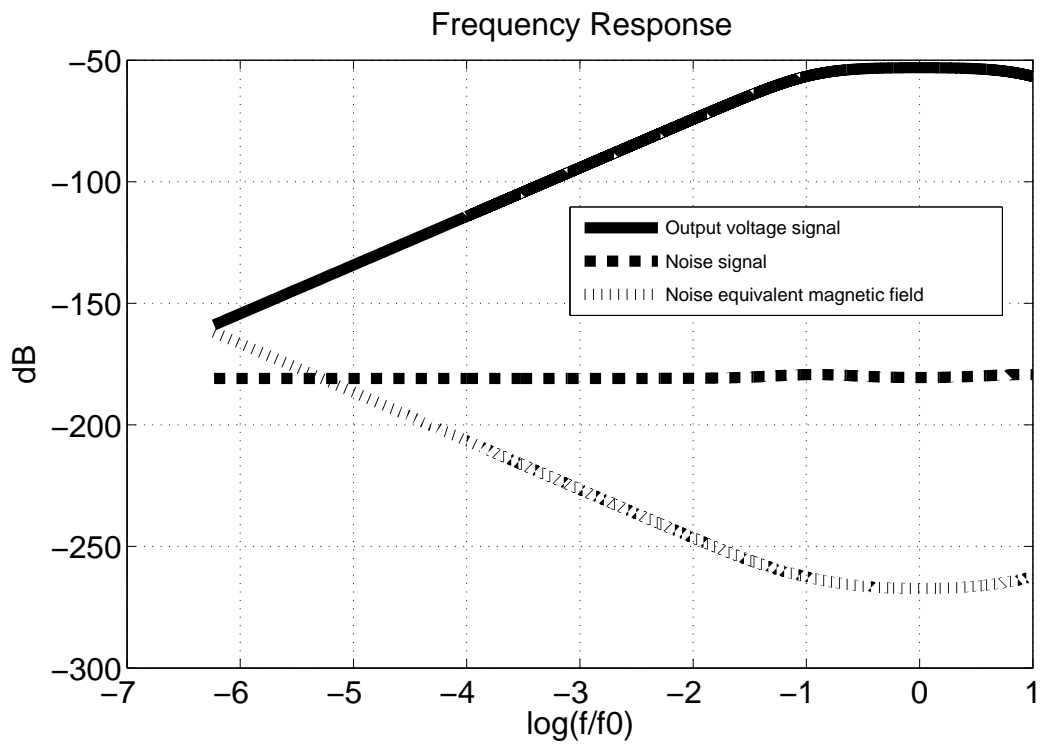


Figure 3.9: Signal, noise and magnetic noise comparison for the first system designed for LFEIT application. Simulation software used is MATLAB. Input magnetic flux density is 1 nT. Amplifier used is AD797. Parallel resistance R_{II} is 100 Ω .

CHAPTER 4

EXPERIMENTAL WORK

4.1 Introduction

In this chapter, the implementation of the designed coil and amplifier combination is presented. Based on the design principles outlined in the previous chapters, two experiments are performed, namely, "Lorentz Field Electrical Induction Tomography" and "Wireless Power Transfer". The circuit schematics for both designs, experimental results and a comparison with the theoretical data is provided.

4.2 Test of the Induction Coil Design

The first experimental work is to test the designed coil in a simple amplifier circuit, to verify the design further before moving on to the biomedical applications.

In this experiment, the input AC magnetic field is given through a transmitter coil system where another induction coil identical to the sensor coil is used to be able to reach more accurate results. The transmitter part is shown in Figure 4.1. Induction coil is connected in series to the function generator and a resistance to control the current flowing through it. The impedance of the coil at the frequency range of interest is composed of inductance and resistance. The resistance and the capacitance of the coil are neglected due to relatively high operation frequency and low coil resistance. Therefore the inductance formula (2.35) can be tested by simply changing the frequency and measuring the peak voltage over the test resistance which is chosen as $1.2k\Omega$. Likewise, the DC resistance formula (2.27) can be tested measuring the resis-

tance of the coil with a multimeter. Both parameters can be obtained experimentally using Agilent E4980A Precision LCR-meter alternatively. Both experimental methods give the same results. The results of the comparison of theoretical inductance and resistance values are given in Table 4.1. The coil designed for LFEIT is referred as coil 1. The coils used in [30] are named coil 2-3, other examples from [31] are the coils 4 and 5. L_{meas} and L_{calc} indicate the measured and calculated inductance values. R_{meas} and R_{calc} are likewise. In Table 4.1 measured and calculated parameters are seen. The discrepancies are mainly due to windings not being as tidy as designed since even a machine is used to wind the coil, it will only increase the speed of winding process. This causes the turn number for same coil size and wire diameter to differ from calculations which leads to changes in the resistance and inductance values. The measurement results indicate that equations used to obtain the inductance and resistance of the coil are accurate with 20-30 percent deviation.

This experiment led to an important correction. The calculation of the turn number, as obtained from equation (2.5), is not accurate in most cases. This is caused by the insulation of the wire. The wire cross-sectional area in resistance equation (2.24) is the area of the conducting part. However while calculating the turn number, this extra thickness from wire insulation need to be included. Then the new turn number becomes:

$$n = l \frac{D - D_i}{2kv^2d^2} \quad (4.1)$$

where v is the ratio of the total wire diameter to the conducting diameter. This is also mentioned in [32]. The equation related to the coil resistance should also be modified as:

$$R_{dc} = \frac{(D + D_i)(D - D_i)l}{\sigma v^2 d^4} \quad (4.2)$$

Note that after these corrections, the results matched with 20-30 percent deviation.

The next stage is to determine the self capacitance of the coil in order to find the location of the resonance frequency. There are again two experimental methods to obtain the self capacitance of an induction coil and three equations are available for

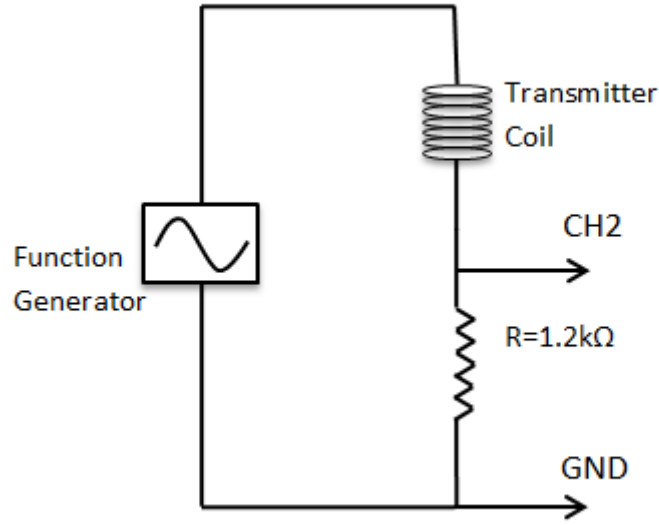


Figure 4.1: Transmitter coil circuit. Signal given from function generator is measured on 1.2 kΩ resistance in order to determine the current through the transmitter coil later to be used in (2.47) to calculate the input magnetic field of the sensor.

designing purposes which are mentioned in the previous chapters. In this part however the equation that performs best will be determined through comparison with the results obtained using experimental methods. First method is to find the resonance frequency of the coil using oscilloscope, then using the obtained resistance and inductance of the coil to get the capacitance. Second method is actually an improved version of the first one. It includes connecting two different external test capacitors to the coil and comparing the resonance frequency of the system for both cases. The advantage of using this method is that the inductance and resistance information is not required. However, the first method will be used to determine the capacitance because the resonance frequency of the coil is also of interest. Equation for calculating the capacitance of the coil is [33]:

$$C = C_1 \frac{\frac{C_2}{C_1} \left(\frac{f_2}{f_1}\right)^2 - 1}{1 - \left(\frac{f_2}{f_1}\right)^2} [pF] \quad (4.3)$$

The coils used in this experiment are coil 1 and 4 from Table 4.1. The results are pre-

Table 4.1: Comparison of theoretical and measured inductance/resistance values for different coils.

Parameter	Coil 1	Coil 2	Coil 3	Coil 4	Coil 5
l(m)	0.0025	0.005	0.005	0.007	0.002
D(m)	0.02	0.03	0.03	0.05	0.03
D_i (m)	0.004	0.007	0.007	0.015	0.01
d(mm)	0.6	0.06	0.5	0.45	0.1
n	70	10000	200	300	1000
L_{meas}	31 μH	1.22 H	361 μH	2.6 mH	21 mH
L_{calc}	27 μH	1.14 H	320 μH	2.2 mH	17.3 mH
R_{meas}	0.2 Ω	3.5 k Ω	1.02 Ω	3.8 Ω	157 Ω
R_{calc}	0.155 Ω	3.22 k Ω	0.79 Ω	3.22 Ω	132 Ω

sented in Table 4.2. The capacitances calculated using (2.40), (2.41) and (2.42) are referred as C1, C2 and C3, respectively. f_1 , f_2 and f_3 are the resonance frequencies calculated using these capacitances, respectively. C_{exp} is the capacitance obtained using f_0 , the experimentally determined self resonance frequency of the coil. Note that when calculating the capacitance, the additional 20 pF emerging from the oscilloscope probe at the measurement side is also included.

Table 4.2: Comparison of the theoretical and experimental capacitance values and resonance frequencies for different coils.

Parameter	Coil 1	Coil 4
l(m)	0.0025	0.007
D(m)	0.02	0.05
D_i (m)	0.004	0.015
d(mm)	0.6	0.45
n	70	300
C1	110.1 pF	108.8 pF
C2	62 pF	62 pF
C3	14 pF	11.6 pF
f_1	2.69 MHz	290 kHz
f_2	3.81 MHz	382 kHz
f_3	5.31 MHz	605 kHz
C_{exp}	76 pF	77 pF
f_0	2.80 MHz	330 kHz

It is observed that the capacitance value C2 which is calculated using equation (2.41) is closer to the measured capacitance value. However due to the discrepancies in

the inductance calculation, capacitance $C1$ that is calculated using (2.42) results in a much more accurate resonance frequency, namely $f1$. This means that the discrepancy in capacitance compensates the inductance error returning a resonance frequency value closer to the experimentally measured f_0 . The accuracy in obtaining the resonance frequency is more critical, therefore (2.41) is slightly more advantageous and used in design.

Next part presents an experiment to compare the measured voltages with the theoretically calculated values. To conduct this experiment, the circuit illustrated in Figure 4.1 is used as the transmission stage where the transmitter coil has the same properties as the receiver coil. Selected coil for the experiment is the coil 1 whose properties are given in the first column of Table 4.1. The receiving stage is shown in Figure 4.2 R and L values are given in Table 4.1. In this configuration, because the amplifier has a high input impedance, the transfer function F of the coil could be modified. Parallel resistance used is $4.1 \text{ k}\Omega$ and parallel capacitance is 2 pF .

Input magnetic field of the receiving stage B is calculated using equation (2.52). Then using this input, output voltage is calculated using MATLAB software. Theoretical and experimental results are given in Table 4.3 (i.e., coil 1). The output voltage for different measurement distances (existing between transmitter and receiver coils) are compared through this experiment. The measurements are obtained at the coil self resonance frequency (2.8 MHz). V_{meas} is the experimental and V_{calc} is the calculated output voltage of the sensor.

Table 4.3: Measured and calculated voltage output for different magnetic field input at respective measurement distances

Parameter	d1=2 cm	d2=1.75	d3=1.5 cm	d4=1.25 cm	d5=1 cm
B	16 nT	19.5 nT	27.1 nT	41.6 nT	67.4 nT
V_{meas}	$0.27 V_{pp}$	$0.32 V_{pp}$	$0.45 V_{pp}$	$0.64 V_{pp}$	$0.81 V_{pp}$
V_{calc}	$0.31 V_{pp}$	$0.38 V_{pp}$	$0.534 V_{pp}$	$0.82 V_{pp}$	$1.3 V_{pp}$

There is significant discrepancy between the results which further increase with the closer measurement distance. To visualize these data and the discrepancy better, Figure 4.3 is obtained. This difference is mainly caused by the effect of mutual coupling

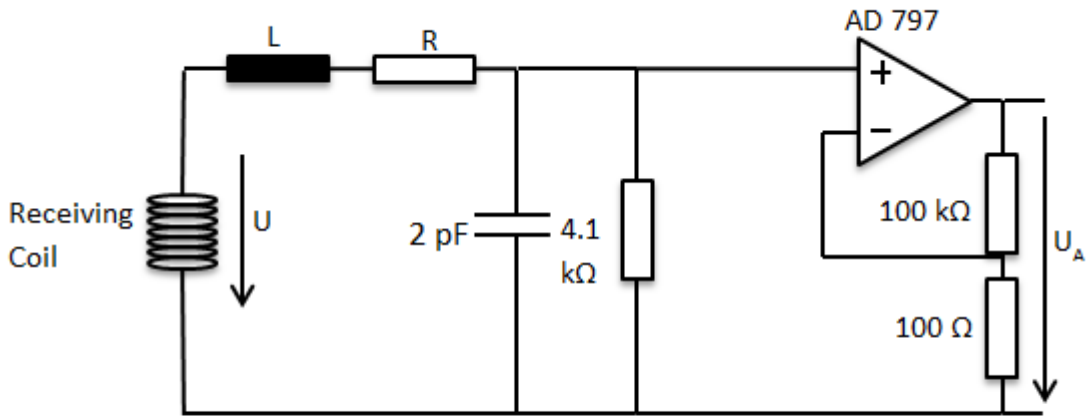


Figure 4.2: Receiver stage. Low noise high input impedance amplifier AD 797 is used.

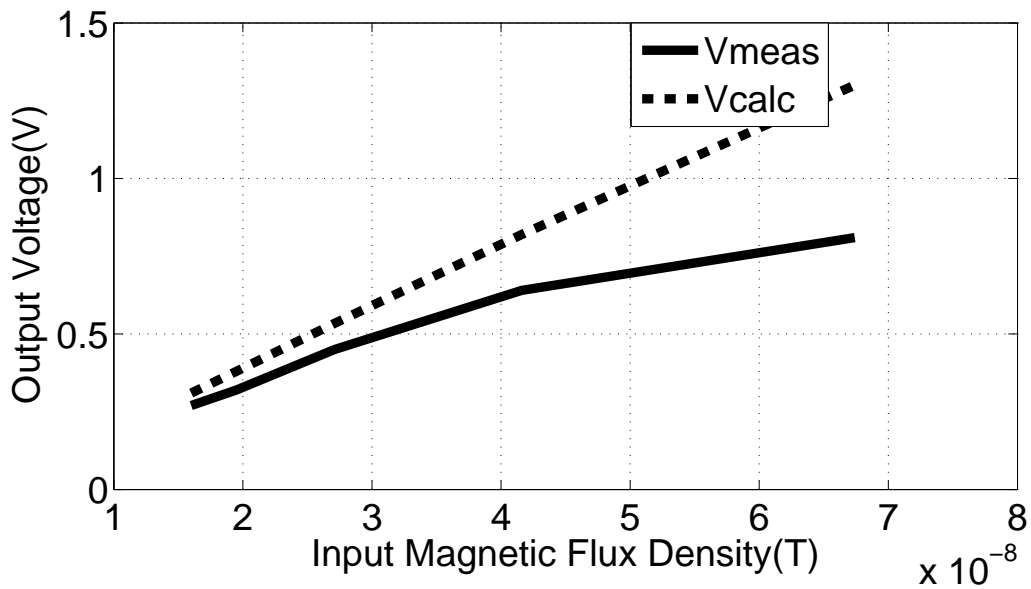


Figure 4.3: Comparison of the theoretical and measured output voltages for a range of magnetic flux density values (on the order of nT) as given in Table 4.3. The operation frequency is 2.8 MHz.

coefficient on inductance that should be included because of the existence of a transmitter coil in order to create input magnetic field. This not only affects the sensitivity directly, but also changes it due to the slight change in the resonance frequency. To show this, mutual coupling for every distance value is measured and the calculation results are modified accordingly as $L_{actual} = M + L$ where M represents the mutual inductance. The corrected set of output voltage values along with the respective coupling coefficients are given in Table 4.4.

Table 4.4: Measured and calculated voltage outputs after modification of inductance by including mutual inductances and respective coupling coefficient value measurements

Parameter	d1=2 cm	d2=1.75	d3=1.5 cm	d4=1.25 cm	d5=1 cm
B	16 nT	19.5 nT	27.1 nT	41.6 nT	67.4 nT
V_{meas}	0.27 V_{pp}	0.32 V_{pp}	0.45 V_{pp}	0.64 V_{pp}	0.81 V_{pp}
V_{calc}	0.28 V_{pp}	0.34 V_{pp}	0.47 V_{pp}	0.65 V_{pp}	0.84 V_{pp}
k	0.062	0.063	0.065	0.09	0.15

As observed, the coupling coefficient becomes almost constant when the distance between the coils is higher than 1.5 cm. However, some discrepancy is still not cleared. This is due to calculation of the input magnetic field using equation (2.52). It should be noted that B is obtained through calculation however it was not verified using an experimental technique. This second reason for the discrepancy is caused by the assumption of uniform flux across the coaxial solenoids. Although coils were placed coaxially in order to obtain smooth comparison between measured and calculated values, the measurement results can only be approximately accurate due to assumptions calculating input magnetic field. Table 4.4 also shows that the output voltage of a designed induction coil magnetic field sensor can be approximately determined without experimental work.

The linearity performance of the sensor is analyzed using the least squares best fit straight line method. This method fits the input output characteristics on an optimum line by selecting the minimum squares of the differences between linear fit and actual values. First step is to determine the slope of the best linear approximation. It is done by taking n data points and then using the following formula:

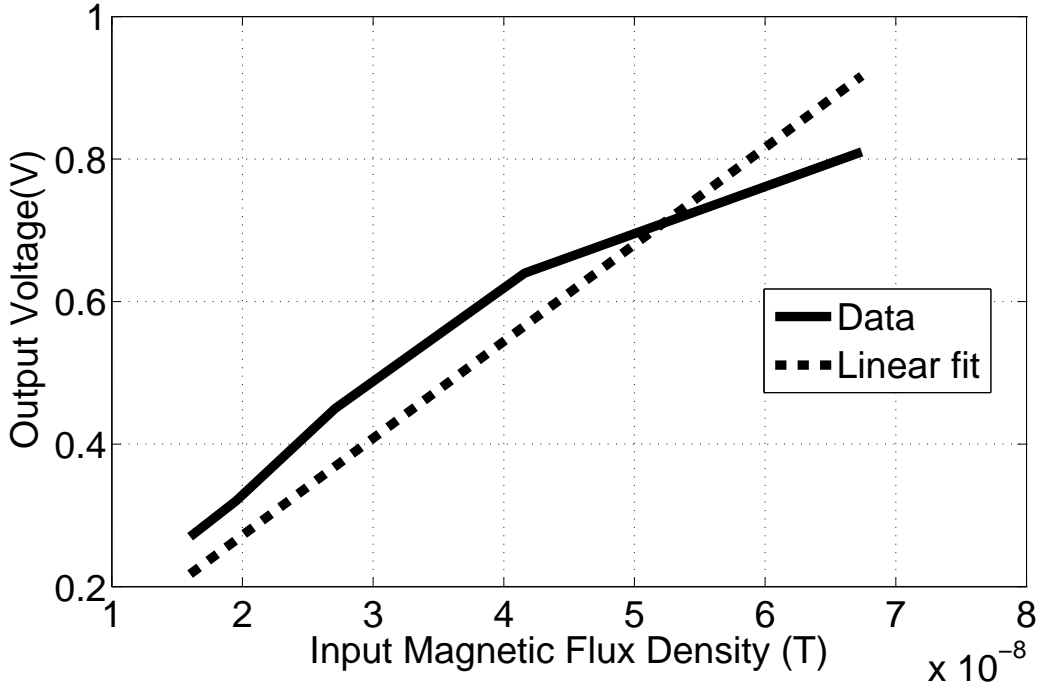


Figure 4.4: Data obtained through measurement and its linear approximation

$$m = \frac{\sum_{k=1}^n X_k Y_k}{\sum_{k=1}^n X_k^2} \quad (4.4)$$

where m is the slope, X_k and Y_k representing the input and output data points respectively. After mathematically determining the slope of the best fit straight line, it is then possible to obtain the maximum deviation percentage of any point from this line using the equation:

$$\%d = \frac{Y_k - mX_k}{mX_{fr}} \quad (4.5)$$

where X_{fr} is full working range of the input data. According to (4.4), the linear approximation obtained is shown in Figure 4.4. The approximated sensitivity can be obtained by multiplying the slope of the line with μ_0 . Sensitivity of the magnetic field sensor (output voltage/magnetic field intensity) is computed as 17.1 (V m/A). The maximum deviation from linearity is calculated using equations (4.4) and (4.5). It occurs at 67.4 nT magnetic flux density (0.0536 A/m magnetic field intensity) and is %15.3. The aim of this part was to verify whether it is possible to determine the output voltage of an induction coil sensor and amplifier combination with the aid of

a design software. The next section will include the optimization of both coil and amplifier using the software mentioned in this section.

4.3 LFEIT Application

The details about LFEIT are given in the introduction chapter. This section will mainly focus on the experimental work relating to LFEIT. As mentioned before, LFEIT aims to reconstruct the conductivity distribution of body using the magnetic fields of ultrasonically induced electrical currents. Thus, a strong amplifier ($A=10000-100000$) and an induction coil with high sensitivity are required. The contribution of this study to the LFEIT application is to design the optimum coil for given circumstances.

The experimental setup includes two magnets producing DC magnetic field horizontally while an ultrasound source is introduced to the system vertically (perpendicular to the magnetic field axis). The system is illustrated in Figure 4.5 [15]. A test tube including two immiscible substances with different conductivities, namely salt water and oil in this case, is attached to the mid section of the system. The sensor coil is placed next to the tube over the boundary area of the two liquids. The important observation here would be the maximum area that sensing can be done. The induction coil sensor diameter will be limited by the tube diameter. If the sensor area is greater than the source area, then S in equation (2.6) is determined by the smaller of the two, rendering a portion of the sensor useless. Therefore there is an upper limitation to the coil diameter. In this experiment it is set to 2 cm. This is one of the reasons a maximum coil diameter input parameter is added to the GUI software. There were also a limited variety of wire while conducting the experiment, so maximum wire diameter is also added to the GUI. There may be cases where an upper limitation to the coil length exist or lower limitations to every parameter can also be taken into account according to the type of the application. After considering all the factors, the results of the GUI software is given in Figure 4.13. The numerical input-output part of the GUI is not the source of data for the graphs. The purpose of the graphs is to verify if there is an optimum result for the induction coil. Therefore they are obtained under the condition where a single parameter is varied while others are fixed at their optimum

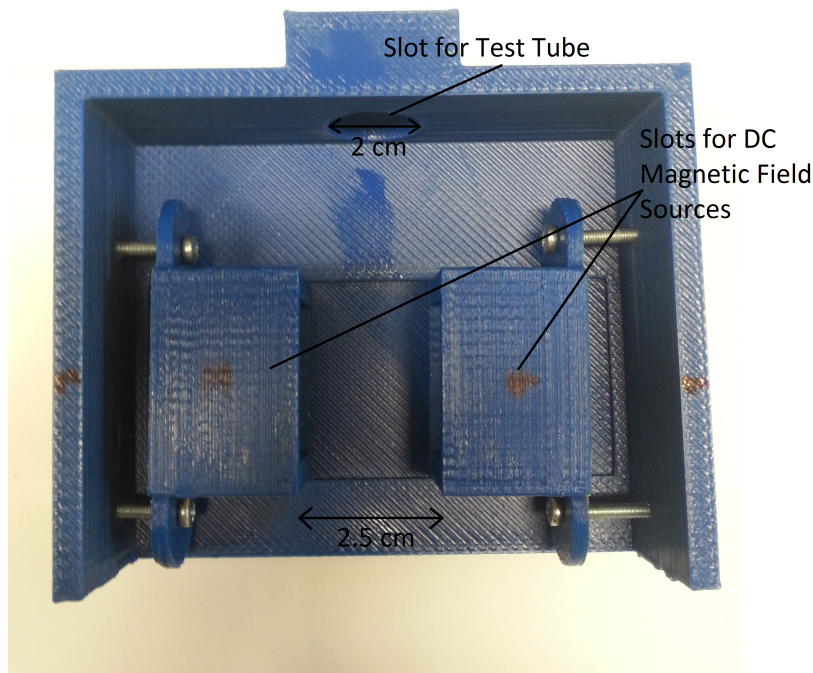
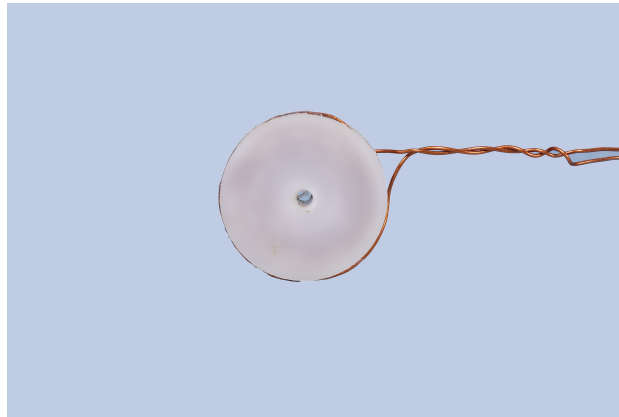


Figure 4.5: Experiment setup without test tube, sensor and ultrasound input, the width of the mid section is greater than the diameter of the test tube and 2.5 cm [15]

values, which are already determined by the GUI. These results are obtained for 10 pT magnetic field input and a gain of 160000 obtained by the chain amplifier circuit designed specifically for this case. The resulting optimum sensor coil is wound and shown in Figure 4.6a and b.

The schematic of the amplifier circuitry is given in Figure 4.9. AD600 is used as amplifier. Its pin configuration and internal structure is illustrated in Figure 4.11. Two AD600 are connected using TL072 as buffer in the first stage. TL072 is chosen due its bandwidth compatibility with AD600. The second stage includes the amplifier block AU-1291. AD600 is an IC component with low input impedance, causing the adjustment of the transfer function F of the sensor to be challenging. On the other hand, it became possible to adjust the operating frequency band by designing appropriate filters. The circuit board is shown in Figure 4.12. AU-1291 has high input impedance, allowing it to be considered as a first stage in an amplifier chain. However this component can not be classified as low-noise, therefore it is used as second stage. AU-1291 has 63 dB gain which corresponds to 1415. The detailed



(a)



(b)

Figure 4.6: Optimum coil designed for LFEIT application (20 mm coil diameter, 2.5 mm coil height (length), 0.6 mm wire diameter) a) Top view, b) Side view

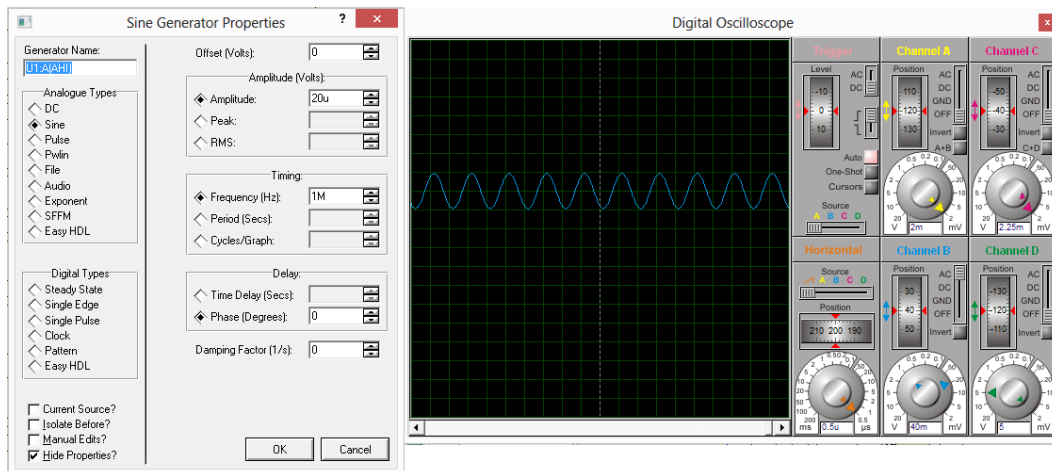


Figure 4.7: Simulation results for the amplifier circuitry designed for LFEIT application. The left hand side shows the input signal characteristics(20 uV, 1 MHz). On the right hand side, the output signal is observed at channel B. The amplification can be calculated as $40\text{mV}/20\text{uV}=2000$. Input signal (channel A) is too small to be revealed on the oscilloscope screen.

schematic of the first stage of the amplifier circuit is given in Figure 4.10. As observed from the schematic, a high pass filter of cutoff frequency 723 kHz is added between the AD600 and buffers to adjust the bandwidth of the system. A low pass filter is not necessary for the application since the frequency of interest is around 1 MHz for LFEIT application. The total amplification factor gained from this circuit is actually greater than 160000. However as the gain increases to a value around 130 dB, it is observed that the input signal to be given for test purpose is below the noise value. Therefore the signal that is observed at the output included significant noise due to the amplification of the noise. As a solution, the second AD600 is excluded in the experiments, leading to an amplification factor of 160000 (104 dB). This amplifier circuit is tested using the simulation software of PROTEUS. The results for the two AD600 case are shown in Figure 4.7. This suggests that if this circuit is used as amplifier as it is, with the additional gain from the second stage total gain will reach $2000*1415=2830000$. This corresponds to 129 dB. Results for the case with second AD600 excluded is given in Figure 4.8. The total amplification including the cascaded second stage is $112.5*1415=159200$. Therefore in the design simulations, 160000 is used.

The input signal is given through the function generator Agilent HP33120A in the

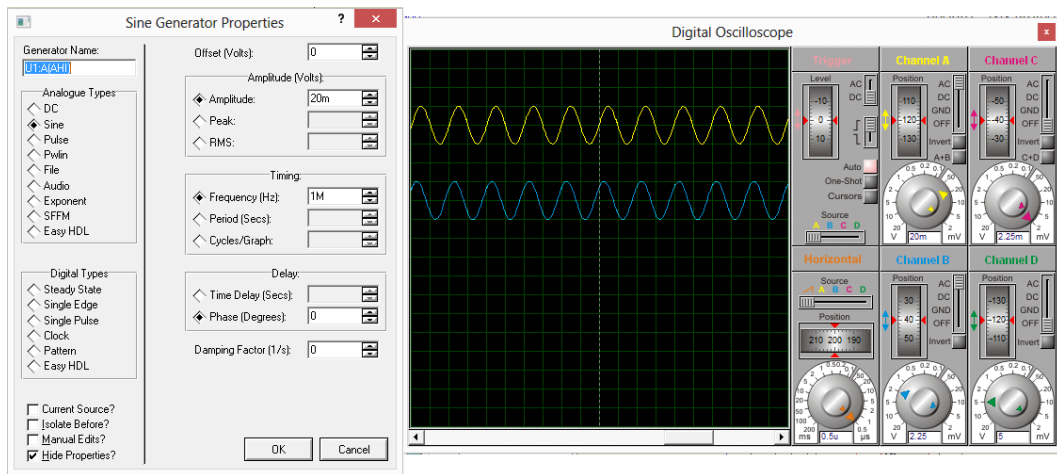


Figure 4.8: Simulation results for the amplifier circuitry designed for LFEIT application(second AD600 excluded). The left hand side shows the input signal characteristics (20 μ V, 1 MHz). On the right hand side, the output signal is observed at channel B. The amplification can be calculated as $2.25/20\text{mV}=112.5$. Input signal (channel A) is also shown on the oscilloscope screen and it is 20 mV in amplitude.

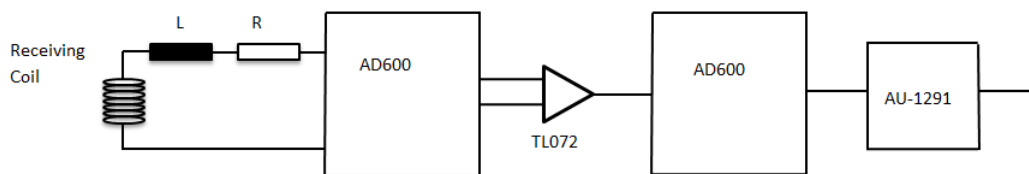


Figure 4.9: Amplifier circuitry designed for LFEIT application

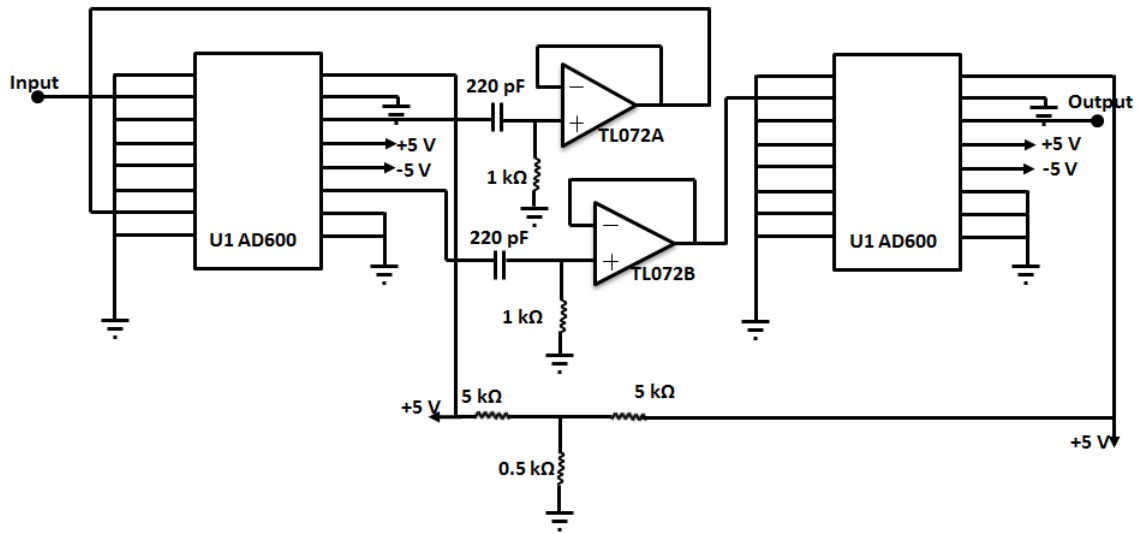


Figure 4.10: The detailed schematic of the first stage of the amplifier circuit

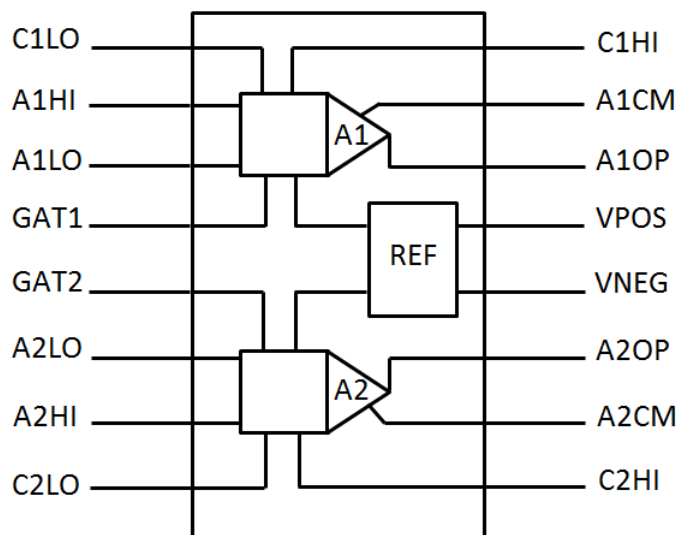


Figure 4.11: Pin configuration and internal structure of AD600

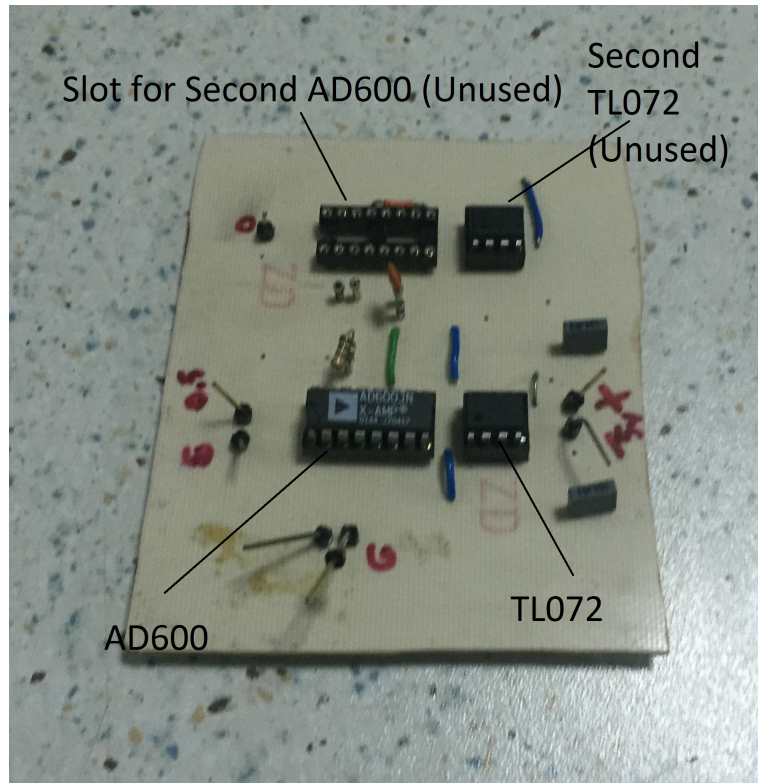


Figure 4.12: The amplifier circuit board

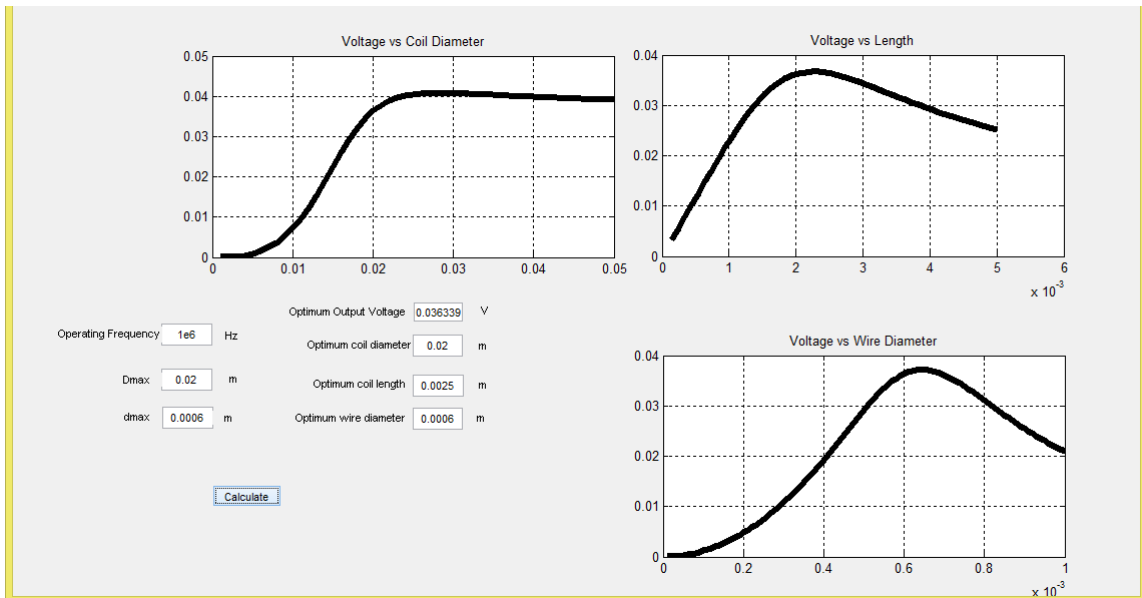


Figure 4.13: GUI results for LFEIT application (with 10 pT input and maximum coil and wire diameter constraints)

form of 1 MHz 3 cycles sinusoid bursts at a pulse repetition frequency of 50 Hz. This signal is amplified using the RF power amplifier. Afterwards it is sent to a 1 MHz 20 mm in diameter transducer focused at 50 mm. The ultrasound pressure was 1 MPa at the focal point. A cylindrical test tube of diameter 20 mm and height 100 mm is placed in the middle of the experiment setup. This test tube is filled with a mixture of salt water and oil, each filling half of the tube. The magnetic field is introduced from both sides by two identical magnets, centering the focal point with a magnitude of 0.5 T.

GUI results given in Figure 4.13 are based on 10 pT input as indicated. However, this magnetic field is induced at the center of the boundary of two liquids inside the test tube. Therefore the magnetic field at the surface of the tube decreases to 0.1 pT. Therefore after administering new input magnetic flux density to the simulation, results shown in Figure 4.15 are obtained. The output voltage is reduced in magnitude by a factor of 100 and the coil parameters are the same as expected. Output voltage is computed as 0.37 mV. However this simulation is done using a wire diameter constraint of 0.6 mm. The case where the wire diameter is not limited is also investigated by adjusting the maximum wire diameter parameter to a greater value. The GUI results for this case are given in Figure 4.16. These new results suggest that the output voltage can be further increased to 0.7 mV by using a 1.6 mm diameter wire and using a 2 cm length coil.

The schematic of the final version of the whole experiment setup is given in Figure 4.19. Expected results are as shown at the introduction part and they are also shown with better quality in Figure 4.20. Two high amplitude signals on the sides are phase inverted and the smaller signal in the middle is to be detected by the magnetic sensor. However, the waveforms obtained at the experiment results are in the form of Figure 4.21. After not being able to distinguish a signal from the noise, an analysis using (3.3) inside MATLAB software gives the results illustrated in Figure 4.22. The bandwidth Δf is calculated as 42 kHz. Resonance frequency f_0 of the overall system is 1.287 MHz. The comparison of the output signal without the amplification and the noise shows that it is not possible to distinguish the signal from noise level with any amount of amplification. However if the input magnetic flux density is increased to 10 pT, the output signal of the sensor can be observed. Figure 4.23 shows that the

signal is barely above the noise level around the frequency of interest (1 MHz). Input spectral noise density of AD600 is given as $1.4nV/\sqrt{Hz}$ which actually becomes the dominant factor in system noise. The reason that the second AD600 is excluded from the system is related to this noise doubling for two AD600 and since noise level is already critical, it should be minimized.

The sensor designed to use in LFEIT application along with the amplification circuitry is also tested in terms of sensitivity and linearity. Using the same arrangement from the previous section, an identical test coil is used to generate AC magnetic field at distances from 1 cm to 2 cm. Output is obtained without amplifier block circuitry (Amplification factor $A=112.5$) The results include the data set for the target operating frequency (1 MHz). They are shown in Table 4.5. The linearity performance of the sensor is illustrated in Figure 4.14. Maximum deviation from linearity is %2.7 at the 1 cm distance which is the closest. Again as in the case of test system constructed in the previous section, linearity gets distorted as the measurement distance decreases. The sensitivity with amplification factor of $A=112.5$ is computed as 5.45 (V m/A). This indicates that in terms of sensitivity, this system performs worse than the test case since the measurements are already done at the resonance frequency. This is due to low input resistance of AD600 amplifier which has a negative effect on the system. However it was chosen in order to be compatible with AU-1291 since very high amplification at 1 MHz operating frequency was required for the application.

Table4.5: Measured voltage outputs at two different frequencies of importance for a range of measurement distance and respective coupling coefficient values

Parameter	d1=2 cm	d2=1.75	d3=1.5 cm	d4=1.25 cm	d5=1 cm
B	16 nT	19.5 nT	27.1 nT	41.6 nT	67.4 nT
$V_{f=1MHz}$	0.072 V_{pp}	0.088 V_{pp}	0.122 V_{pp}	0.184 V_{pp}	0.286 V_{pp}
k	0.062	0.063	0.065	0.09	0.15

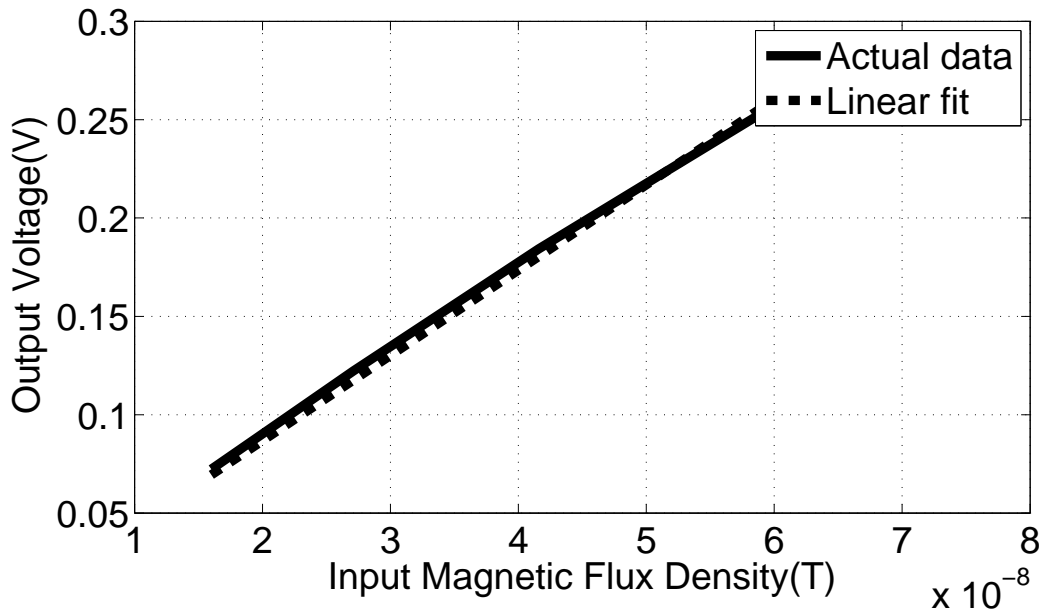


Figure 4.14: Data obtained through measurement and its linear approximation

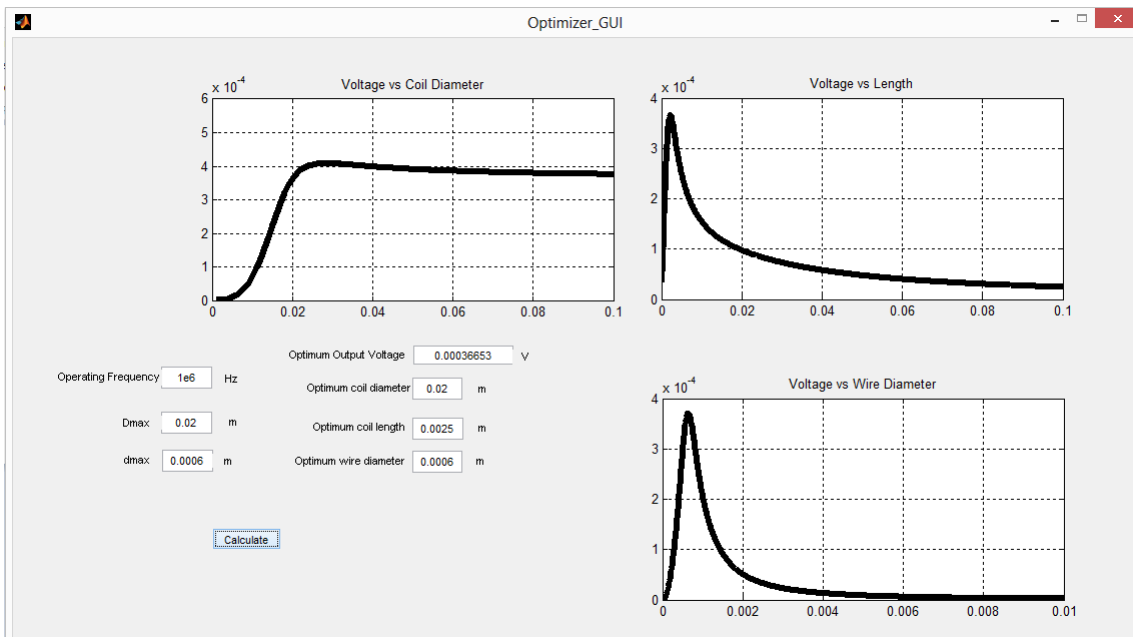


Figure 4.15: GUI results for LFEIT application with 0.1 pT input and maximum coil diameter and wire diameter constraints of 2 cm and 0.6 mm respectively. Operation frequency is 1 MHz. Output voltage is calculated as 0.37 mV. Optimum coil length is computed as 2.5 mm. Wire diameter of the optimized coil is 0.6 mm.

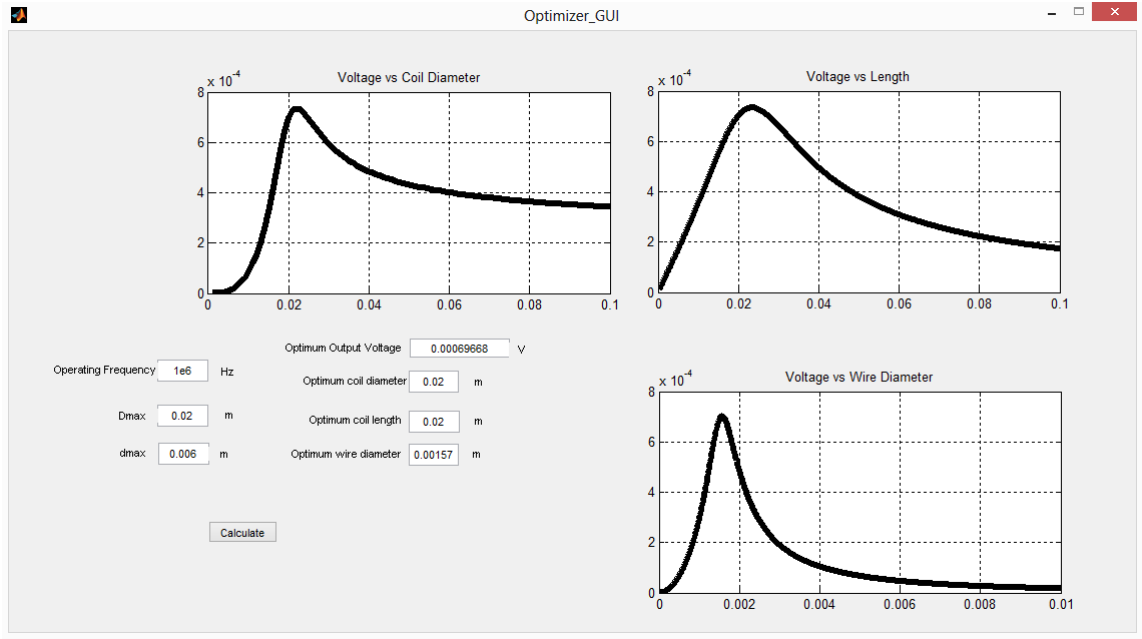


Figure 4.16: GUI results for LFEIT application with 6 mm wire diameter constraint. This value is chosen high enough to check whether there is a better coil if there were no wire diameter constraint. Output voltage for the determined optimum coil is calculated as 0.7 mV. Wire diameter is computed as 1.57 mm. Optimum coil length is also changed and it is 2 cm.

4.4 Wireless Power Transfer (WPT) Application

Although WPT is a form of magnetic sensor application, it requires a different approach. In magnetic sensor applications, the goal is to maximize the voltage sensitivity. However in WPT, it is necessary to maximize the power transfer. To achieve this, the efficiency should be maximum. It is given for two coil system in equation [34], [35], [36]:

$$\eta = \frac{k^2 Q_p Q_s}{1 + k^2 Q_p Q_s} \quad (4.6)$$

where η is the efficiency, k is the mutual coupling between the coils and Q_p and Q_s are the quality factor of the primary and secondary coils respectively. However, the low Q-factor especially observed under loaded condition and the low coupling between the coils, two coiled system has relatively low efficiency. This efficiency also decreases exponentially with the distance between coils. This limits the maximum distance both coils could be placed from each other. Therefore four coiled system is preferred. The schematic of such design is given in Figure 4.24 where all the

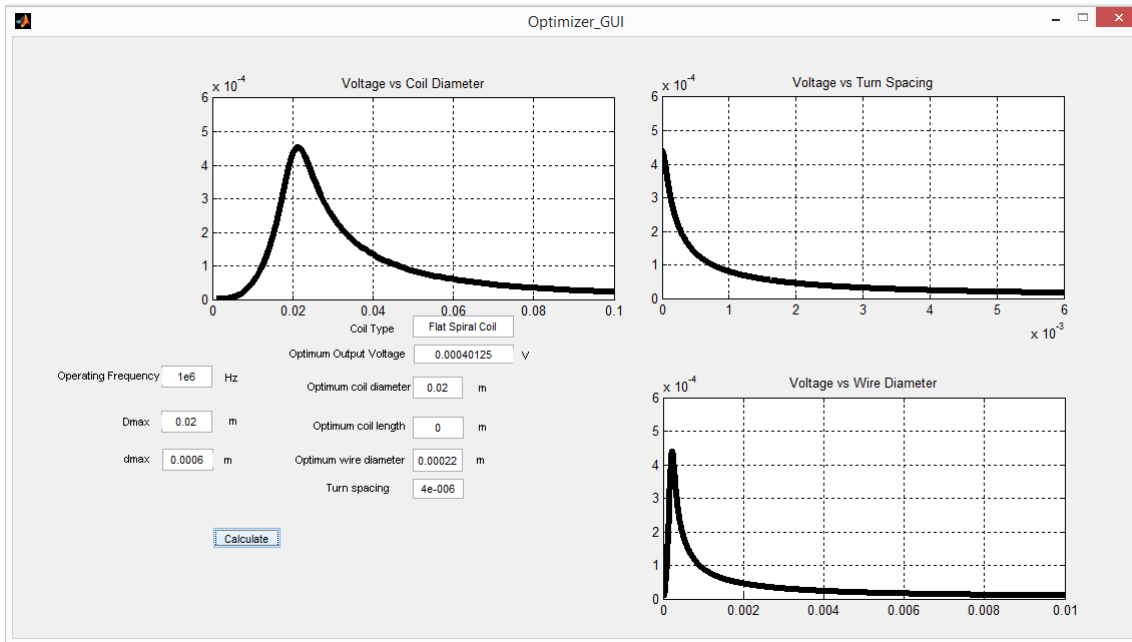


Figure 4.17: Improved GUI results for LFEIT application with 0.6 mm wire diameter constraint. Improved GUI includes additional software that determines whether flat spiral coil or air-cored multilayer coil performs better. It is observed that a flat spiral coil provides a slightly better output voltage (0.4 mV) compared to the results given in Figure 4.15. Since the optimum coil type is determined as flat spiral, instead of coil length parameter, the turn spacing parameter is included. Wire diameter of the optimum coil is calculated as 0.2 mm and the turn is spacing is 0.004 mm.

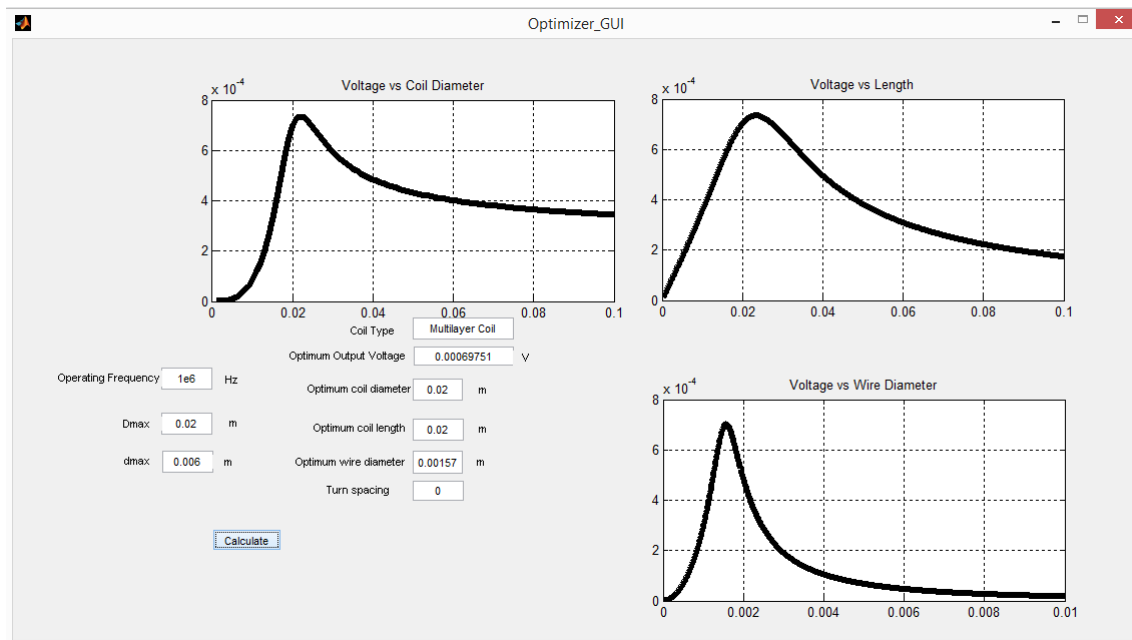


Figure 4.18: Improved GUI results for LFEIT application with 6 mm wire diameter constraint. The results are same as in Figure 4.16 since the optimum coil type for this case is air-cored multilayer coil.

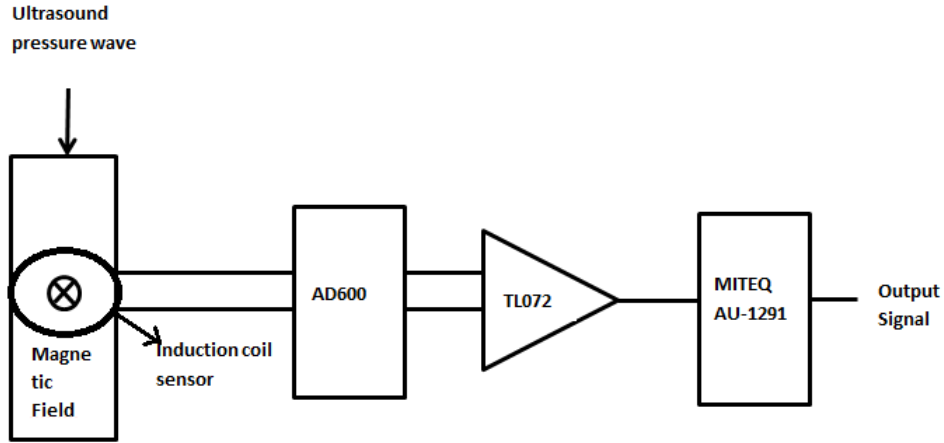


Figure 4.19: The schematic of the final version of the experiment setup. Dc magnetic field is seen at inward direction which is perpendicular to the measurement axis. Induction coil sensor is placed adjacent to the tube in order to obtain best sensitivity performance.

parameters illustrated will be used in its efficiency equation [37], [38], [39], [40]:

$$\eta = \frac{(k_{12}^2 Q_1 Q_2)(k_{23}^2 Q_2 Q_3)(k_{34}^2 Q_3 Q_4)}{[(1 + k_{12}^2 Q_1 Q_2)(1 + k_{34}^2 Q_3 Q_4) + k_{23}^2 Q_2 Q_3][1 + k_{23}^2 Q_2 Q_3 + k_{34}^2 Q_3 Q_4]} \quad (4.7)$$

where k_{mn} is the coupling factor between coil m and coil n, and Q_m is the quality factor of coil m. Equation (4.7) is valid assuming all coils are tuned to the same resonance frequency and operating at this frequency. Also for this equation to hold, coupling coefficients between nonadjacent coils k_{13} , k_{14} and k_{24} should be negligible compared to the coupling coefficients between adjacent coils. Since the interaction between nonadjacent coils would be weaker, equation (4.7) performs better as the distance between primary and secondary coils increases. Coupling factor k has a value between 0 and 1. It is 1 for two identical coils placed next to each other. However as the geometry of the coils differ and as they become more distant, k decreases. Since the distance between Tx and Rx coils is relatively greater, their coupling coefficient k_{23} is small compared to k_{12} and k_{34} . Hence the quality factors of these coils Q_2 and

Electrical signal

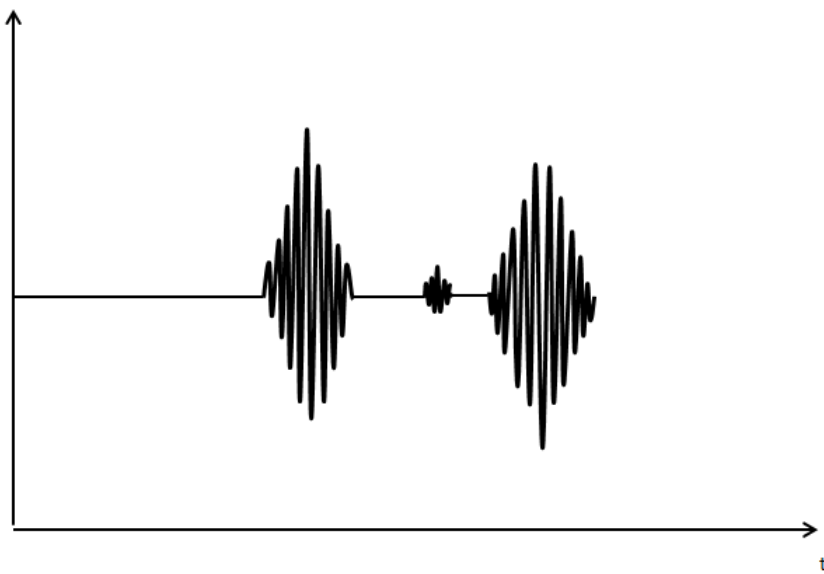


Figure 4.20: The illustration of expected results of the experiment. The scale among the signals to be measured is represented in this figure. The signals with greater amplitude correspond to outer boundaries with higher conductivity gradient namely the boundary between air and oil, salt water and tube respectively. These expected signals are out of phase 180 degrees. The waveform in the middle corresponds to the conductivity gradient between salt water and oil therefore it is smaller. The aim is to observe this smaller signal since it will prove whether the conductivity difference between two different tissues can be distinguished.

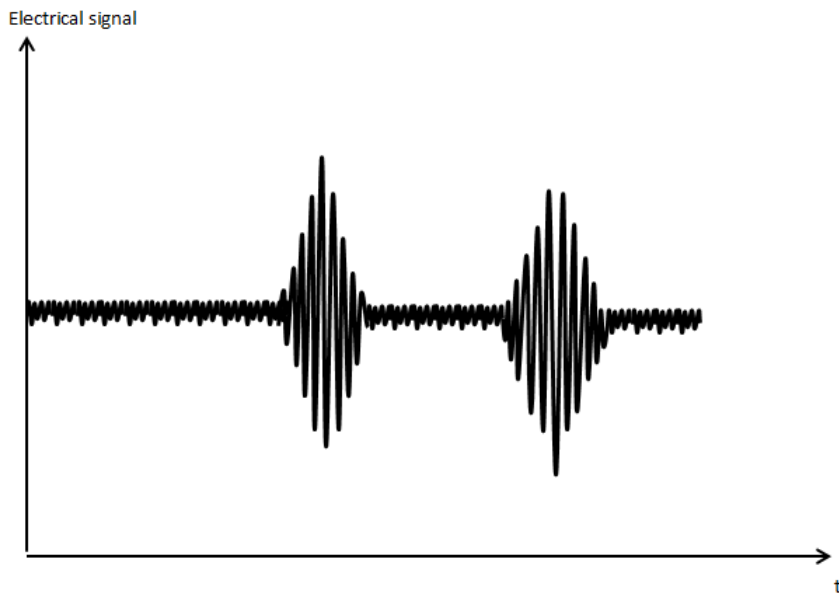


Figure 4.21: The illustration of results of the experiment. The outer boundary signals are obtained at a scale of 5 V. However the noise signal obtained is greater than the expected inner boundary waveform, therefore it was not possible to distinguish this signal from the noise.

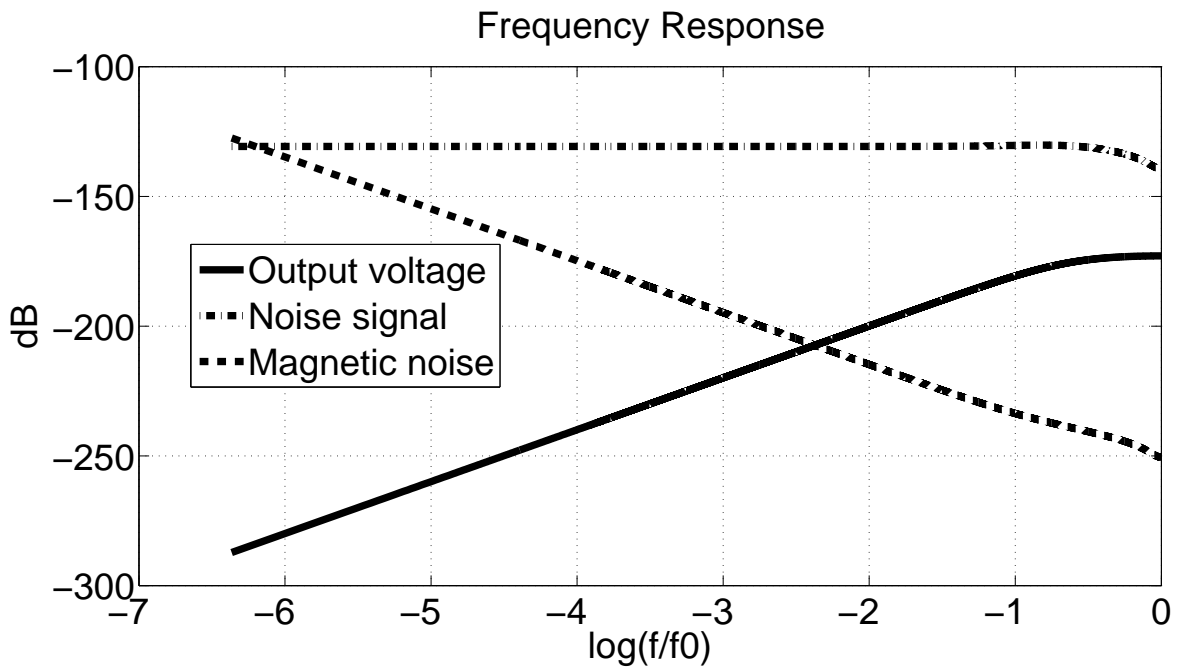


Figure 4.22: Theoretical results for noise analysis of the experiment setup for 0.1 pT input magnetic flux density. It is observed that the output voltage of the sensor is below the noise level.

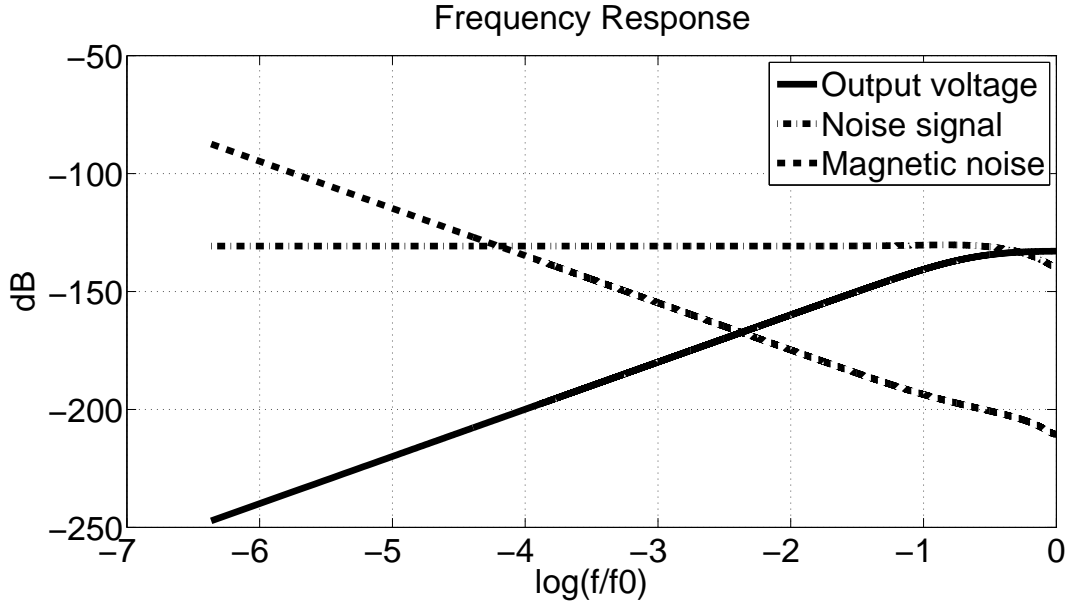


Figure 4.23: Theoretical results for noise analysis of the experiment setup for 10 pT input magnetic flux density. This simulation indicates that if it is possible to increase the input flux density by using a higher magnitude DC field or placing the sensor closer to the source with a different configuration, output signal reaches above the noise level at the resonance frequency.

Q_3 are required to be maximized in order to compensate the reduction in the efficiency caused by low coupling. In order to achieve this, the optimization algorithm designed in the previous sections is modified into determining the coil parameters for maximum quality factor.

The quality factors of driving and load coils (Q_1 and Q_4 respectively), cannot reach the level of unloaded Q_2 and Q_3 because of source and load resistances. Therefore their effects on efficiency are limited. Q of an unloaded coil is:

$$Q = \frac{2\pi f L_{eff}}{R} \quad (4.8)$$

where R is the total resistance and L_{eff} is the effective inductance which is obtained by:

$$L_{eff} = L \left(1 - \left(\frac{f}{f_0} \right)^2 \right) \quad (4.9)$$

f_0 is the self resonance frequency of the coil as mentioned in the sections before. Therefore quality factor also depends on the operating frequency. To determine this frequency, the structure of overall system and its relation with human body should

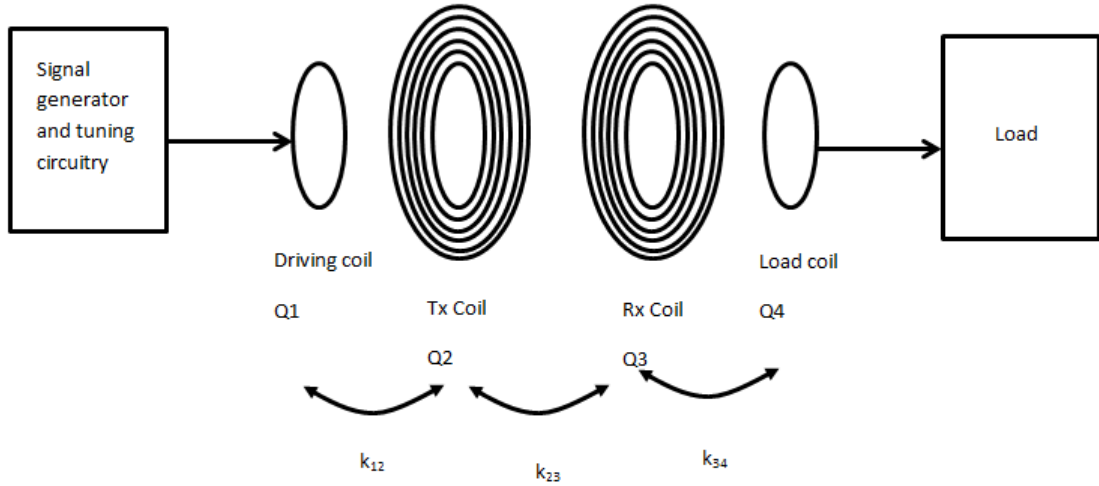


Figure 4.24: Four coil wireless power transfer system. In the figure, k_{mn} is the coupling factor between coil m and coil n , and Q_m is the quality factor of coil m

be considered. The receiver coil, as mentioned, is to be placed inside the tissue. The permeability of the tissue can be assumed to be close to free space [41]. This indicates that the coil inductance inside a tissue will not be affected. However, the tissue has high dielectric constant [42], [43], and hence, introduces more capacitance to the system. This further reduces the quality factor of the implanted coil, which has relatively small size causing its capacitance to be small. Therefore a possible tuning capacitor at the receiving end has very little effect on operating frequency of the system. The tissue and the high frequency magnetic field is rather close to each other, resulting in tissue absorbing part of magnetic field input due to the eddy current generation. This absorption is lower for a frequency range of 100 kHz-4 MHz, leading to an improvement in the efficiency due to minimizing the effects of tissue. Operating frequency of a wireless power transfer system to be used in biomedical applications should be in this range. For this application, 1 MHz is chosen due to practical reasons.

The distance between the transmitter and receiver coils is determined using the equation (2.52). To maximize B_x , $a = \rho\sqrt{2}$ condition should be met. This means that in order to maximize the magnetic field transfer, the diameter of the transmitter coil should be chosen as $D = 2\sqrt{2}\rho$.

It is not possible to accurately model the coupling factor between two multilayer coils, therefore it is measured experimentally. The method is as follows: The inductance of the primary coil is measured while the secondary coil is under open circuit and short circuit conditions. Then using the equation:

$$k = \sqrt{1 - \frac{L_s}{L_o}} \quad (4.10)$$

where L_s indicating the primary coil inductance for short circuited secondary coil and L_o indicating the open circuited secondary.

The optimization algorithm from previous section is also used here to obtain coil parameters for maximum Q. Calculated and measured quality factors of selected coils and their size parameters are given in Table 4.6. LCR meter is used to measure the quality factor parameter. The loaded quality factors are not measured, only calculated due to discrepancy being relatively low. In the table, it can also be seen that the calculation of the multilayer coil resistance using Dowell method, results are accurate with the resistance measurement with some discrepancy.

Table 4.6: Size parameters of the coils with optimum quality factor

Parameter	Coil 1	Coil 2	Coil 3	Coil 4
Coil Outer Diameter(D)-mm	30	25.5	17	20
Coil Inner Diameter(D_i)-mm	25.5	6	4	17
Coil Length(l)-mm	5	5	2.5	2.5
Wire Diameter(d)-mm	1	1	0.6	0.6
Number of Turns	8	36	44	12
Inductance(L) μ H	3.4	13.4	15.8	4.4
Calculated Resistance(R_{calc}) Ω	1.5	3.77	6.35	2.57
Measured Resistance(R_{meas}) Ω	1.87	4.5	6.25	2.85
Q(calculated-loaded)	0.216	17	13	0.16
Q(measured)	11.5	18	12.7	9.7

Using the method indicated above, k_{12} is found as 0.62, k_{23} is 0.0675, k_{34} is 0.55 for 8.5 mm distance and 1 MHz operating frequency for the selected coils. Then using (4.5) since all the parameters included are revealed, the efficiency is calculated as %6.8. Coil 1 is loaded with 5.6 Ω in series to represent the source impedance and coil

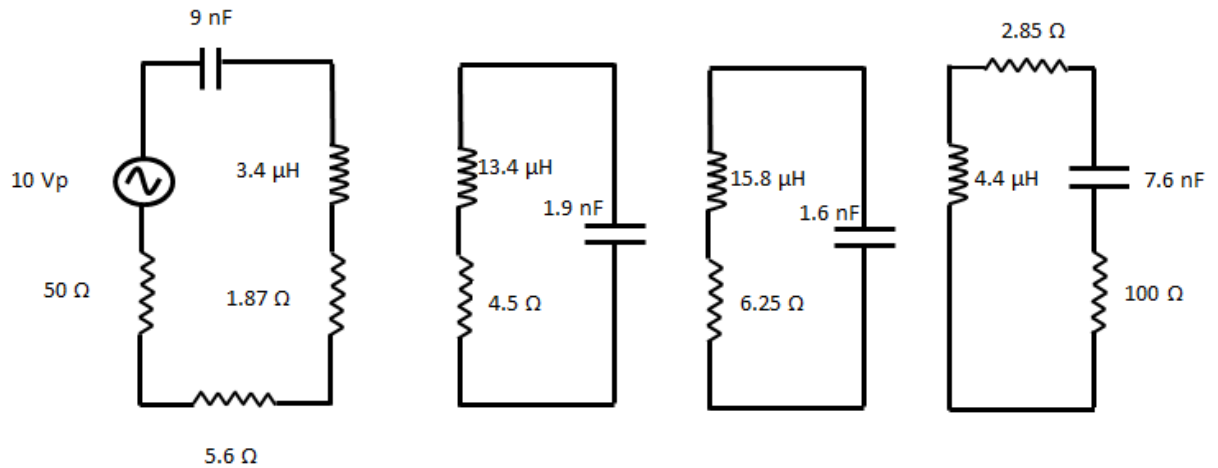


Figure 4.25: Four coil wireless power transfer system circuitry schematic including components with their respective values

4 is loaded with 100Ω in series to represent the load. The schematic of the whole circuitry is given in Figure 4.25

The coil 3 of the selected coils is the one used as induction coil sensor in LFEIT application in the previous section. The optimum coil parameters were actually, $D=2$ cm, $l=0.3$ cm, $d=0.06$ cm and $D_i=0.4$ cm. However since there is no significant difference in quality factor, the sensor coil from LFEIT application is used as the receiver. Coil 2 on the other hand, is newly designed for this application. It is shown in Figure 4.26a and 4.26b as top view and side view. The driver and load coils are concentric with the transmitter and receiver coil respectively by forming the outermost layers of them.

The driver coil and load coil are designed with relatively low turn number due to the fact that their quality factor will be already small due to loading. Their inductance values are also of importance since they need to resonate at the selected operating frequency which is 1 MHz for this case. The tuning capacitance can be calculated



(a)



(b)

Figure 4.26: Optimum quality factor coil designed for WPT application (30 mm coil diameter, 5 mm coil height(length), 1 mm wire diameter) a) Top view, b) Side view

using:

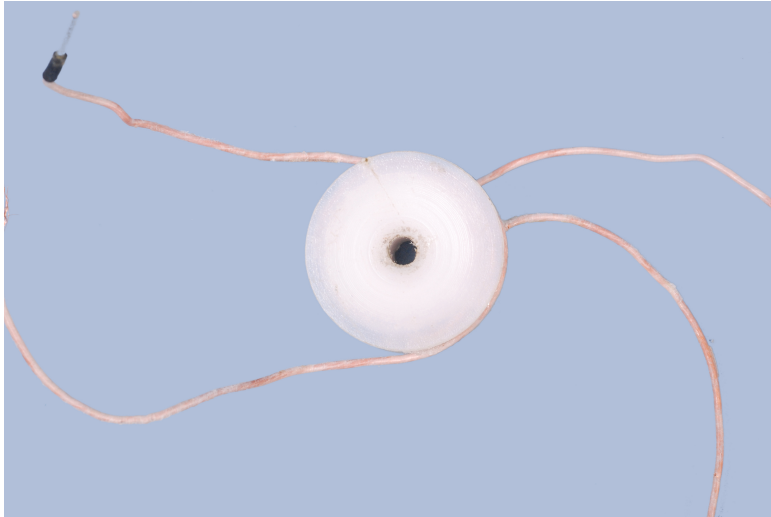
$$j\omega L - \frac{1}{j\omega C} = 0 \quad (4.11)$$

$$C = \frac{1}{(2\pi f)^2 L} \quad (4.12)$$

The inductance of the driver coil is $3.4 \mu H$ and the load coil is $4.4 \mu H$. Therefore the tuning capacitances for driving and load parts are 9 nF and 7.6 nF respectively. The tuning capacitances of primary and secondary coils are close being 1.9 nF and 1.6 nF respectively. Remembering the condition $D = 2\sqrt{2}\rho$, the distance between the coils is adjusted as 8.5 mm. Afterwards the experiment setup included the four coil system, specified tuning capacitances and load resistances connected to driving and load coils in series. Input signal given has 1 MHz frequency and 10 V_{peak} amplitude and as the load, 100Ω is connected in series. The input power is measured as 0.15 Watts, which is inversely proportional with the load impedance seen by the source. The output voltage on the 100Ω is measured as 1.5 V_{peak}, using average power equation $P = \frac{V^2}{2R}$, leading to an output power of 0.0113 Watts. Therefore the efficiency calculated using measurement values is %7.7. This shows that although the efficiency is low in this case, the discrepancy of the design is also low. The reason for low output power is the low input power transfer from voltage source which has 50Ω internal resistance.

The efficiency can be improved by using litz wires which provide significant improvement in coil quality factor. Litz wire is composed of many wire strands. It increases quality factor by providing very low resistance compared to regular copper wire. To prove this, the windings of primary and secondary coils mentioned are changed to 1 mm diameter litz wire with number of strands as 66. The resulting coils have the properties mentioned in Table 4.7. These coils are shown in Figure 4.27a and b.

It is shown that the usage of litz wire as windings increase the quality factor greatly. The coupling coefficients for this case are computed as: $k_{12} = 0.515$, $k_{23} = 0.043$, $k_{34} = 0.43$. Then using (4.7), efficiency is increased up to %13.8. This is verified through implementation by obtaining an output voltage of 2.3 V_{peak} for 0.18 W input power, therefore resulting in %14.7 efficiency. Although by only changing the windings



(a)



(b)

Figure 4.27: Optimum quality factor coil with litz wire windings designed for WPT application (30 mm coil diameter, 5 mm coil height(length), 1 mm wire diameter) a) Top view, b) Side view

Table 4.7: Critical parameters of the coils modified to include Litz wires as their windings

Parameter	Coil 1	Coil 2	Coil 3	Coil 4
Inductance(L) μ H	1.76	3.25	0.53	0.23
Resistance(R_{calc}) Ω	0.19	0.176	0.045	0.047
Q(load)	1.94	134	81	0.015

into litz wire without any coil design process the efficiency is doubled, the resulting efficiency is still relatively weak. This is due to the low loaded quality factor of the load coil. Therefore assuming there is further space for improvement, another secondary coil with better loaded quality factor is wound. The 0.3 mm diameter 40 strand litz wire is used in the windings. The properties of this coil along with its load counterpart is given in Table 4.8.

Table 4.8: Critical parameters of the secondary coil modified further to have high loaded quality factor

Parameter	Coil 3	Coil 4
Inductance(L) μ H	65	41
Resistance(R_{calc}) Ω	23	23
Q(load)	17	2.094

Afterwards, considering mutual coupling coefficient values, k_{12} and k_{34} are measured as same, however k_{23} is measured as 0.052. Then using (4.7), the efficiency is calculated as %37.1. This is again verified as 3.3 V_{peak} is observed on the 100 Ω load at 0.14 W input power resulting in %38.9 efficiency. This is the best efficiency obtained so far, even so the quality factor of the secondary coil is relatively low. It should be noted that in the litz wire winding part of the WPT application, coil design was not required since there were two different types of litz wire available during the experiments. The coil design of WPT application with enamel copper wire can be easily modified to design litz wire coils by changing the resistance and inductance equations. This part is only done to prove that the efficiency can be greatly increased by usage of litz wire.

CHAPTER 5

CONCLUSION AND DISCUSSION

A magnetic sensor system with the best sensitivity under certain circumstances, including an air-cored induction coil connected to an amplifier circuit is designed. A MATLAB based graphical user interface software is developed for this purpose. This software is verified by checking with numerous coils designed for various biomedical applications like MIT or contactless conductivity imaging. The precision of calculations and the discrepancies are investigated thoroughly. The linearity of sensitivity is New parameters such as wire insulation thickness are understood through experimental work. The optimum coil is designed using the present equipment and its parameters are: Diameter(D): 2 cm, length(l): 0.25 cm, wire diameter(d): 0.6 mm, inner diameter(D_i): 0.4 cm. However the performance of the system designed for the LFEIT application is found to be inadequate. This is both due to requirement of very high sensitivity and signal being so small that its level remaining below noise level. The sensitivity can be increased by using another low noise amplifier circuit with high input impedance through placing an adjusting resistance in parallel, but at the cost of bandwidth. One of the suggestions to improve the results would be to find a way to get close to the source. This might be achieved if the sensor coil is placed inside the test tube, by using a wider tube. However fixing its position inside the liquids would be challenge and it would also introduce another boundary area. Another suggestion is to use the improved GUI to determine whether the coil type used is optimum or not. The results of related simulations are given in Figure 4.17. This proves that under the wire diameter limitation, the use of flat spiral coil gives better results. However this is not the case when the wire diameter is not limited as shown in Figure 4.18. Therefore multilayer air cored coil is the optimum coil type choice for LFEIT application

given that all required material such as wire with appropriate diameter is accessible. A noise shielding metal casing is also necessary in the final design of the system in order to minimize the noise from the coil, both thermal noise and interference from the environment, however it is not implemented in this study.

After the LFEIT application, the properties of wireless power transfer is also investigated. Four coil structure is chosen due to having more flexible design constraints. The maximum efficiency of the power transfer is required to be achieved. In order to accomplish this, quality factor of the transmitter and receiver coils should be maximized according to the equation given. To obtain the size parameters of the maximum quality factor, optimization software designed in MATLAB is modified into providing size parameters for the greatest quality factor. Afterwards, coupling factors between the coils are measured by separating coils two by two. Then the tuning capacitances are determined. Finally, the distance of greatest magnetic flux transfer and tuning capacitances for driving and load sides are determined and the system is implemented. Expected efficiency was %6.8, which can be considered as rather poor performance, however the resulting practical efficiency value was obtained as %7.6. Afterwards, litz wires is used at windings instead of enamel copper wire. The efficiency of the system is increased up to %39 through the improvement observed in the coil quality factors.

As an improvement, litz wire coils should be designed in detail in order to increase the quality factor which greatly affect the efficiency of the system, while improving the loaded conditions. As another improvement, there are other coil types than the disk shaped air-cored induction coil such as rectangular coil, ferromagnetic-core coil. These coils can also be optimized for the desired applications since their inductance and capacitance can also be formulated or derived from the air-cored coil. An improvement for wireless power transfer could be the use of coils with better coupling coefficients, especially the coupling between transmitter coil and receiver coil needs improvements. This can be done by making the transmitter and receiver coils' turn number close hence adjust their inductance closer to each other. This application also requires the coils to be shielded by a metal casing, not because of noise this time but in order to prevent the resistance from changing due to temperature. Again this is not implemented, but mentioned as a suggestion to improve the system further, espe-

cially in the final implementation stage. There are also other applications that can be studied such as MIT, contactless conductivity imaging etc. These applications can be studied in detail and suggestions about various types of coil for every application can be made.

REFERENCES

- [1] T. C. Oakberg, “Magneto-optic kerr effect,” *HINDS Instruments*, vol. 1, no. 1, 2005.
- [2] C. M. Falco and I. K. Schuller, “Squids and their sensitivity for geophysical applications,” *SQUID Applications to Geophysics*, pp. 13–18, 1980.
- [3] J. Clarke, “Squid fundamentals,” in *SQUID sensors: fundamentals, fabrication and applications*. Springer, 1996, pp. 1–62.
- [4] J. E. Lenz, “A review of magnetic sensors,” *Proceedings of the IEEE*, vol. 78, no. 6, pp. 973–989, 1990.
- [5] E. Ramsden, *Hall-effect sensors: theory and application*. Newnes, 2011.
- [6] T. Casselman and S. Hanka, “Calculation of the performance of a magnetoresistive permalloy magnetic field sensor,” *Magnetics, IEEE Transactions on*, vol. 16, no. 2, pp. 461–464, 1980.
- [7] W. Kwiatkowski and S. Tumanski, “The permalloy magnetoresistive sensors—properties and applications,” *Journal of Physics E: Scientific Instruments*, vol. 19, no. 7, p. 502, 1986.
- [8] S. Tumanski, “Induction coil sensors—a review,” *Measurement Science and Technology*, vol. 18, no. 3, p. R31, 2007.
- [9] S. A. Macintyre, “Magnetic field measurement,” *ENG Net Base*, 2000.
- [10] G. Dehmel, “Magnetic field sensors: induction coil (search coil) sensors,” *Sensors Set: A Comprehensive Survey*, pp. 205–253, 1989.
- [11] P. Ripka, *Magnetic sensors and magnetometers*. Artech House on Demand, 2001.
- [12] H. Zijlstra, “Experimental methods in magnetism,” 1967.
- [13] R. Prance, T. Clark, and H. Prance, “Compact room-temperature induction magnetometer with superconducting quantum interference device level field sensitivity,” *Review of scientific instruments*, vol. 74, no. 8, pp. 3735–3739, 2003.
- [14] R. Zengin, “Electrical impedance tomography using lorentz fields,” *METU, M. Sc. Thesis*, 2012.
- [15] M. Karadaş, “Development of novel reconstruction algorithms for eit using lorentz fields,” *METU, M. Sc. Thesis*, 2014.
- [16] P. Grasland-Mongrain, J.-M. Mari, J.-Y. Chapelon, and C. Lafon, “Lorentz force electrical impedance tomography,” *IRBM*, vol. 34, no. 4, pp. 357–360, 2013.
- [17] H. Ammari and H. Kang, *Reconstruction of small inhomogeneities from boundary measurements*. Springer, 2004, no. 1846.

- [18] L. Filipczynski, "Absolute measurements of particle velocity, displacement or intensity of ultrasonic pulses in liquids and solids," *Acta Acustica united with Acustica*, vol. 21, no. 3, pp. 173–180, 1969.
- [19] S. Haider, A. Hrbek, and Y. Xu, "Magneto-acousto-electrical tomography: a potential method for imaging current density and electrical impedance," *Physiological measurement*, vol. 29, no. 6, p. S41, 2008.
- [20] A. Montalibet, J. Jossinet, and A. Matias, "Scanning electric conductivity gradients with ultrasonically-induced lorentz force," *Ultrasonic imaging*, vol. 23, no. 2, pp. 117–132, 2001.
- [21] B. Soong, Y. Sum, W. Liu, and S. Ramachandran, "Characterizing wire wound inductor coils for optimized wireless power transfer," in *Advanced Intelligent Mechatronics, 2009. AIM 2009. IEEE/ASME International Conference on*. IEEE, 2009, pp. 469–474.
- [22] P. Si, A. P. Hu, D. Budgett, S. Malpas, J. Yang, and J. Gao, "Stabilizing the operating frequency of a resonant converter for wireless power transfer to implantable biomedical sensors," in *Proc. 1st Int. Conf. Sensing Technology*, 2005, pp. 477–482.
- [23] Y.-M. Gimm, H.-S. Yoo, M.-J. Kim, J.-S. Yoo, and S.-H. Park, "Receiving coil analysis of wireless power transmission with inductive coupling," in *Microwave Conference, 2007. KJMW 2007. Korea-Japan*. IEEE, 2007, pp. 117–120.
- [24] A. P. Sample, D. A. Meyer, and J. R. Smith, "Analysis, experimental results, and range adaptation of magnetically coupled resonators for wireless power transfer," *Industrial Electronics, IEEE Transactions on*, vol. 58, no. 2, pp. 544–554, 2011.
- [25] V. G. Welsby, *The theory and design of inductance coils*. Macdonald, 1950.
- [26] Y. Lee, "Antenna circuit design," *Application manual of Microchips Technology*, 1999.
- [27] P. Dowell, "Effects of eddy currents in transformer windings," *Electrical Engineers, Proceedings of the Institution of*, vol. 113, no. 8, pp. 1387–1394, 1966.
- [28] H. A. Wheeler, "Simple inductance formulas for radio coils," *Radio Engineers, Proceedings of the Institute of*, vol. 16, no. 10, pp. 1398–1400, 1928.
- [29] A. Massarini and M. K. Kazimierczuk, "Self-capacitance of inductors," *Power Electronics, IEEE Transactions on*, vol. 12, no. 4, pp. 671–676, 1997.
- [30] L. E. M. ÇOLAK, "An improved data acquisition system for contactless conductivity imaging," Ph.D. dissertation, MIDDLE EAST TECHNICAL UNIVERSITY, 2005.
- [31] K. Ö. Özkan, "Multi-frequency electrical conductivity imaging via contactless measurements," *METU, M. Sc. Thesis*, 2006.
- [32] E. C. Snelling, "Soft ferrites," 1969.
- [33] Q. Yu and T. W. Holmes, "A study on stray capacitance modeling of inductors by using the finite element method," *Electromagnetic Compatibility, IEEE Transactions on*, vol. 43, no. 1, pp. 88–93, 2001.
- [34] A. Kumar, S. Mirabbasi, and M. Chiao, "Resonance-based wireless power delivery for implantable devices," in *Biomedical Circuits and Systems Conference, 2009. BioCAS 2009. IEEE*. IEEE, 2009, pp. 25–28.

- [35] L. Rindorf, L. Lading, and O. Breinbjerg, "Resonantly coupled antennas for passive sensors," in *Sensors, 2008 IEEE*. IEEE, 2008, pp. 1611–1614.
- [36] M. Catrysse, B. Hermans, and R. Puers, "An inductive power system with integrated bi-directional data-transmission," *Sensors and Actuators A: Physical*, vol. 115, no. 2, pp. 221–229, 2004.
- [37] H. Haus and W. Huang, "Coupled-mode theory," *Proceedings of the IEEE*, vol. 79, no. 10, pp. 1505–1518, 1991.
- [38] A. Karalis, J. D. Joannopoulos, and M. Soljačić, "Efficient wireless non-radiative mid-range energy transfer," *Annals of Physics*, vol. 323, no. 1, pp. 34–48, 2008.
- [39] A. Kurs, A. Karalis, R. Moffatt, J. D. Joannopoulos, P. Fisher, and M. Soljačić, "Wireless power transfer via strongly coupled magnetic resonances," *science*, vol. 317, no. 5834, pp. 83–86, 2007.
- [40] A. K. RamRakhyani, S. Mirabbasi, and M. Chiao, "Design and optimization of resonance-based efficient wireless power delivery systems for biomedical implants," *Biomedical Circuits and Systems, IEEE Transactions on*, vol. 5, no. 1, pp. 48–63, 2011.
- [41] J. Malmivuo and R. Plonsey, *Bioelectromagnetism: principles and applications of bioelectric and biomagnetic fields*. Oxford University Press, 1995.
- [42] M. W. Baker and R. Sarpeshkar, "Feedback analysis and design of rf power links for low-power bionic systems," *Biomedical Circuits and Systems, IEEE Transactions on*, vol. 1, no. 1, pp. 28–38, 2007.
- [43] U.-M. Jow and M. Ghovanloo, "Modeling and optimization of printed spiral coils in air, saline, and muscle tissue environments," *Biomedical Circuits and Systems, IEEE Transactions on*, vol. 3, no. 5, pp. 339–347, 2009.